The Two-Higgs Doublet Model and Sonification: Using Sound to Understand the Origin of Mass

R. Michael Winters
Physics Department
The College of Wooster

A dissertation submitted in partial fulfillment of the requirements of Senior Independent Study in Physics at The College of Wooster

Adviser
Dr. Deva O'Neil

Second Reader
Dr. Brendan Miller

March 15, 2010

Abstract

The Two-Higgs Doublet Model is a well studied extension of the Standard Model of particle physics. Most notably, it predicts the existence of five Higgs particles, three of which are electrically neutral (h_1, h_2, and h_3), a charged particle H^+, and its anti-particle H^-. Contributions of the basis-independent CP-violating Two-Higgs Doublet Model to the oblique parameters S, T, U, V, W, X were calculated. Relationships between the oblique parameters and the five Higgs particles were determined numerically. The effects of adjusting the theoretical upper bounds for Z_1, $\mathrm{Re}(Z_6 e^{-i\theta_{23}})$, $\mathrm{Im}(Z_6 e^{-i\theta_{23}})$, $\mathrm{Re}(Z_5 e^{-2i\theta_{23}})$, $\mathrm{Im}(Z_5 e^{-2i\theta_{23}})$, Z_{34}, and Z_3 by factors of $\frac{1}{10}$, $\frac{1}{2}$, 2, and 10 were studied. Using the original theoretical upper bounds, correlations between S-V-W-m_1, S-V-W-$m_{H^\pm}$, T-U-X-m_1, and T-U-X-$m_{H^\pm}$ were sonified using the sound synthesis program SuperCollider.

Acknowledgments

I would like to thank Dr. Deva O'Neil for her help and guidance in understanding and applying the Two-Higgs Doublet Model. In addition to her insightful teaching, her enthusiasm for the application of Sonification to this research was tremendously helpful. I'd also like to thank Dr. Hermann and especially Florian Grond of the Ambient Intelligence Group at Bielefeld University for their direction as experts in Sonification and introducing me to SuperCollider. Additionally, I'd like to thank Dr. John Lindner and Dr. Greg Brown for their help and encouragement in [5].

Contents

List of Tables

List of Figures

Chapter 1

Introduction & Motivation

1.1 Extending the Standard Model

The Standard Model (SM) of particle physics, the operational theory of fundamental particles and their interactions, is not expected to provide a complete description of nature. It must be superseded by a theory which incorporates gravitational interactions near the Plank scale (10^{19} GeV), but may also break down at relatively lower energies. Therefore, although the SM has thus far been an effective theory at the energy scale of 1 TeV, it is not expected to be valid for some high energy scale. Various extensions of the SM have been proposed as explanations for observations such as dark matter and theoretical problems such as Grand Unification.

The most popular of these extensions is supersymmetry which provides a mechanism for the source of dark matter. Incorporating supersymmetry into the Standard Model requires doubling the number of particles because each fundamental particle needs a super-partner. In order to account for the lack of experimental evidence for super-partners, theorists have moved towards more complicated versions of supersymmetry. The simplest possible supersymmetric model that is consistent with the SM is the Minimal Supersymmetric Standard Model (MSSM). It requires two Higgs doublets in its scalar sector.

The Two-Higgs Doublet Model (2HDM) is a model of low-energy particle interactions that is equivalent to the Standard Model except for the addition of one extra-Higgs doublet. Although it is implied by MSSM, it functions independently as well. For this and other reasons, it is one of the most studied extensions of the Standard Model. The extended Higgs sector would appear experimentally as five Higgs particles, whereas the Standard Model predicts only one.

1.2 Electroweak Symmetry Breaking in the Standard Model

The nature of electroweak symmetry breaking (EWSB) is one of the most important questions in theoretical particle physics. Although the Standard Model has a mechanism for dealing with EWSB, it has not received experimental confirmation. For reasons addressed in section 1.4, other ways of implementing EWSB are of theoretical interest.

The Standard Model of particle physics is constructed by applying local symmetries to the interactions of fundamental particles. At energies far above the electroweak scale ($\approx$90 GeV), the symmetry group is $SU(3) \times SU(2) \times U(1)$. $SU(3) \times SU(2) \times U(1)$ summarizes the symmetries of the SM in group theoretical notation. $SU(3)$ refers to the three-fold (red/green/blue) color symmetry of the strong force. $SU(2) \times U(1)$ refers to the symmetries of the electroweak force. $SU(2)$ comes from the doublet structure of the particles subject to the weak force, and $U(1)$ is the phase symmetry of electromagnetism which arises after EWSB. Typically, these symmetry groups require a massless gauge boson (force-carrying particle) corresponding to each generator of the symmetry group. Thus the $SU(2) \times U(1)$ symmetry group requires 4 massless force-carrying particles. However, when the universe evolved to lower energies, this symmetry was spontaneously broken producing masses for the three gauge bosons of the weak nuclear force ($W^{\pm}$, and Z^0), and leaving the force carrier for electromagnetism (the photon) massless.

Thus, spontaneous symmetry breaking requires the existence of a field (the Higgs field) that permeates space and has non-zero vacuum energy. A particle acquires mass when it interacts with this field. This process is known as the "Higgs Mechanism." The energy associated with this interaction is the vacuum expectation value v. If this scalar field exists, it can be used to explain why particles such as fermions have mass.

1.3 Generating Fermion Masses

The fundamental problem of electroweak symmetry breaking is the nature of mass within the fermion sector. Fermions (i.e., electrons, neutrinos, and quarks) are the elementary particles associated with matter, but without the Higgs mechanism there is no known mechanism which would allow these particles to be massive within the framework of the Standard Model. The Higgs field couples with the massless quark and lepton fields generating mass. By generating masses for the fermions (and gauge bosons), the Higgs mechanism provides the Standard Model with an explanation for the data observed in current particle accelerators.

The effects of electroweak symmetry breaking are evident in the fermion sector. In addition to other intrinsic properties, fermions experience either a left-handed or right-handed helicity. Helicity h is the projection of the spin $\vec{S}$ onto the direction of momentum $\hat{p}$ defined by

$$h = \vec{S} \cdot \hat{p}. \tag{1.1}$$

By convention, particles with a negative helicity are "left-handed," and particles with positive helicity are "right-handed."

The effects of electroweak symmetry breaking are different in the lepton and quark sectors. In the lepton sector, after electroweak symmetry breaking left-handed leptons always appear in SU(2) doublets, while right-handed leptons will always appear in singlets. This creates a problem for calculating mass terms from the Lagrangian. To illustrate the problem, mass terms for the electron will serve for an example. In the Lagrangian, left-handed electrons will always appear in SU(2) doublets:

$$E_L = \begin{pmatrix} \nu_e \\ e^- \end{pmatrix}_L. \tag{1.2}$$

where ν_e is the neutrino and e^- is the electron. However, there are no right-handed neutrios, so right-handed electrons e_R are singlets. Because there are no right-hand doublets, terms in the Lagrangian which we would expect to generate mass terms, such as

$$m_e \bar{e}_R e_L + m_e \bar{e}_L e_R \tag{1.3}$$

where m_e is the mass of the electron, are strictly forbidden. Therefore, to generate the mass of these leptons, one needs a scalar SU(2) doublet ϕ that interacts with left and right handed leptons. This doublet ϕ is the Higgs doublet. Mass terms in the Lagrangian would therefore become

$$\eta^E \bar{E}_L \cdot \phi e_R + h.c. \tag{1.4}$$

where η^E is a dimensional coupling constant, and h.c. stands for hermitian conjugate. After ϕ acquires a vacuum expectation value v, a mass term can be read from the Lagrangian

$$\frac{v}{\sqrt{2}} \eta^E \bar{e}_L e_R + h.c., \tag{1.5}$$

where $m_e = \frac{1}{\sqrt{2}} \eta^E v$. This model can be extended to all three generations of leptons (electron-like particles). In summary, it is not possible to have a mass term for fields with a doublet structure without the Higgs doublet.

In the quark sector, it is possible to have a right handed doublet, but without the Higgs field, there is an apparent asymmetry in the masses. Experimentally, quarks of different flavor have different masses despite being of the same generation. For example, the up quark has a mass of 1.5-3.3 MeV and the down quark have a mass of of 3.5-6.0 MeV. However, with the Higgs field, an analogous calculation to Eqn. (1.5) can be made for quarks. Using an expanded 3-dimensional model which takes into account the mixing of quark generations, the mass of the up quark M_U and down quark M_D can be written

$$M_U = \frac{v}{\sqrt{2}}\eta^U \qquad M_D = \frac{v}{\sqrt{2}}\eta^{D\,\dagger}, \tag{1.6}$$

where η^U and $\eta^{D\,\dagger}$ are matrices that give the strength of the interaction between the Higgs particle and the quarks. The vacuum expectation value for the Higgs particle is therefore a feature of the mass terms of all fermions.

1.4 The CP-Violating Two-Higgs Doublet Model

CP (Charge-Parity) symmetry states that the laws of physics would be the same if a particle was switched with its anti-particle and left and right handedness were also exchanged. A theory without this property violates CP. In 1964, CP-violation was experimentally verified through the decay of neutral kaons into their antiparticles [7]. Experimenters James Cronin and Val Fitch noticed that the transformation did not occur with exactly the same probability in both directions, showing that nature does not treat left-handed particles the same as right-handed anti-particles.

It has been shown that the Standard Model can explain CP violation by incorporating complex values into the CKM (Cabibbo-Kobayashi-Maskawa) matrix. The CKM matrix is a numerical 3x3 matrix whose values are experimentally determined. Each element of the CKM matrix M_{ij} represents how strongly an up-like quark q_i interacts with a down-like quark q_j. It can be used to explain theoretically why the top quark is more likely to decay into a bottom quark than to a down or strange. A CKM matrix with strictly real values will exhibit no CP-violation.

By adopting complex values for the CKM, the Standard Model provided a sufficient theoretical explanation for the experimental evidence of CP-violation. However, an underlying problem of the SM is that it is not believed to be sufficient to explain antimatter. The universe contains far more matter than antimatter and the CKM matrix is only a small feature of the Standard Model. The solution to this apparent radical asymmetry is one of the great unsolved problems in contemporary particle physics. The Two-Higgs Doublet Model provides a possible source for CP-violation and, paired with a theory of supersymmetry, provides a dark matter candidate as well.

Although supersymmetry requires a multi-Higgs doublet model, the Two Higgs Doublet Model is independent of supersymmetry. It is identical to the Standard Model in all respects except the inclusion of one extra Higgs doublet. While the Standard Model's single Higgs doublet is sufficient to explain electroweak symmetry breaking, it does not allow for CP-violation. The 2HDM not only explains EWSB, but also provides another possible source for CP violation.

Chapter 2

The Basis-Indpendent CP-Violating 2HDM

2.1 Basis-Independent Formalism

The following section summarizes the work of Haber and O'Neil [1].

As featured in the MSSM, the two Higgs doublets can be described by a parameter $\tan\beta$,

$$\tan\beta \equiv \frac{v_2}{v_1} \equiv \frac{\langle \Phi_2^0 \rangle}{\langle \Phi_1^0 \rangle}, \tag{2.1}$$

which describes how much of the vacuum expectation value v_1, v_2 is in the first doublet and how much is in the second. However, in the most general 2HDM, this quantity is not well-defined because one can perform a basis transformation that changes how much of the vacuum expectation value appears in each doublet. Therefore, it is important to define the parameters of the theory so that they are "invariant," meaning that they do not depend upon the basis choice of the Higgs doublets. In this section, the details of the basis-independent 2HDM will be developed.

Different bases in the 2HDM have varying distributions of the vacuum expectation value between the doublets. For the 2HDM independent of MSSM, there is no way to tell in advance what the symmetries are that will constrain the scalar sector and the definition of physical parameters must be defined in the most generic implementation of the 2HDM. To explain experimentally observed quantities in terms of the physical parameters of the general model, one needs a way to relate ambiguous or pseudo-invariant parameters to invariant parameters. Only invariant parameters can be candidates for observable quantities because observables should not depend upon the choice of basis (the distribution of the vacuum expectation value).

Without loss of generality a drastic simplification is to place the vacuum expectation value in the first Higgs doublet. Therefore we define H_1 and H_2

such that

$$< H_1 >= \frac{v}{\sqrt{2}}\,, \qquad\qquad < H_2 >= 0, \tag{2.2}$$

where v is the vacuum expectation value. Defining generic doublets as H_1 and H_2, under a generic $U(2)$ transformation they transform to another pair H_1' and H_2' as

$$H_1' = H_1\,, \qquad\qquad H_2' = e^{i\chi} H_2\,, \tag{2.3}$$

where χ parameterizes the phase of the class of Higgs basis being used. Specifically the unitary matrix

$$U_D \equiv \begin{pmatrix} 1 & 0 \\ 0 & e^{i\chi} \end{pmatrix} \tag{2.4}$$

transforms any unprimed Higgs basis to a primed basis. As desired, H_1, the doublet which contains the vacuum expectation value, is invariant of basis, while H_2 is pseudo-invariant.

Using H_1 and H_2, it is possible to write the most general gauge invariant scalar potential as

$$\begin{aligned} \mathcal{V} \;=\; & Y_1 H_1^\dagger H_1 + Y_2 H_2^\dagger H_2 + [Y_3 H_1^\dagger H_2 + \text{h.c.}] + \tfrac{1}{2} Z_1 (H_1^\dagger H_1)^2 \\ & + \tfrac{1}{2} Z_2 (H_2^\dagger H_2)^2 + Z_3 (H_1^\dagger H_1)(H_2^\dagger H_2) + Z_4 (H_1^\dagger H_2)(H_2^\dagger H_1) \\ & + \left\{ \tfrac{1}{2} Z_5 (H_1^\dagger H_2)^2 + \left[Z_6 (H_1^\dagger H_1) + Z_7 (H_2^\dagger H_2) \right] H_1^\dagger H_2 + \text{h.c.} \right\}, \end{aligned} \tag{2.5}$$

where Y_1, Y_2, and $Z_{1,2,3,4}$ are invariant quantities and Y_3 and $Z_{5,6,7}$ are pseudo-invariants. Notice that the coefficients for the quadratic and quartic terms for the doublets are invariant whereas the other terms are pseudo-invariant. The invariant coefficients are all real whereas the pseudo-invariants are potentially complex. The freedom of phase (χ) in Eqn. 2.3 results in other pseudo invariants in the scalar potential. The substitution

$$Y_1 = -\tfrac{1}{2} Z_1 v^2\,, \qquad\qquad Y_3 = -\tfrac{1}{2} Z_6 v^2\,, \tag{2.6}$$

is a result of minimizing the scalar potential (Eqn. 2.5). Only invariants can be candidates for observable quantities. However, combining two pseudo invariant quantities results in an invariant. For example,

$$|Z_5| = \sqrt{Z_5 Z_5^*} = \sqrt{Z_5 e^{i\chi} Z_5^* e^{-i\chi}} = \sqrt{|Z_5|^2}, \tag{2.7}$$

which is independent of phase χ.

From the pseudo-invariant coefficients, one can form four independent real invariants $|Y_3|$, $|Z_{5,6,7}|$ and three invariant relative phases $\arg(Y_3 Z_5^*)$, $\arg(Y_3 Z_6^*)$ and $\arg(Y_3 Z_7^*)$. Including the 6 invariants from Eqn. (2.5), this leaves eleven invariant quantities in the basis-independent 2HDM parameter space. One of these is the vacuum expectation value v.

2.2 The Physical Higgs Mass-Eigenstates

The Two-Higgs Doublet Model has five observable Higgs particles regardless of whether it is CP violating or conserving. The doublet scalar fields of the Higgs basis are parametrized as

$$H_1 = \begin{pmatrix} G^+ \\ \frac{1}{\sqrt{2}}\left(v + \varphi_1^0 + iG^0\right) \end{pmatrix}, \qquad H_2 = \begin{pmatrix} H^+ \\ \frac{1}{\sqrt{2}}\left(\varphi_2^0 + ia^0\right) \end{pmatrix}, \tag{2.8}$$

with hermitian conjugates

$$H_1^\dagger = \begin{pmatrix} G^- & \frac{1}{\sqrt{2}}\left(v + \varphi_1^0 + iG^0\right) \end{pmatrix}, \qquad H_2^\dagger = \begin{pmatrix} H^- & \frac{1}{\sqrt{2}}\left(\varphi_2^0 + ia^0\right) \end{pmatrix}, \tag{2.9}$$

where $G^\pm$ is the charged Goldstone boson pair and G^0 is the CP-odd neutral Goldstone boson. Before EWSB, the Goldstone bosons were observable as propagating particles. However, at this point in the evolution of the universe, the Goldstone bosons are observable only indirectly as the masses of the Z^0 and $W^\pm$ bosons. The neutral Goldstone boson G^0 becomes the mass of the Z^0 boson while $G^\pm$ becomes the mass of the $W^\pm$ particle. If the Higgs sector is CP-conserving, then a^0 will be a mass eigenstate. If the Higgs sector is CP-violating, then φ_1^0, φ_2^0, and a^0 mix to form three additional physically observable particles. Because $H^\pm$ do not mix with φ_1^0, φ_2^0, and a^0 in Eqn. 2.5, $H^\pm$ will become manifest as mass eigenstates regardless. Mass eigenstates will appear as states of definite mass and therefore observable particles. φ_1^0, φ_2^0 will always mix, and therefore cannot be mass eigenstates or states of definite mass.

To determine the mass of these particles, one needs to first examine the terms of the scalar potential (Eqn. 2.5) that are quadratic in the scalar fields. Quadratic and linear terms are relevant because the requirement that the coefficient for linear terms vanishes corresponds to minimizing the scalar potential and results in the simplification used in Eqn. (2.6). Furthermore, because no quadratic terms involving the Goldstone bosons survive, we know that the Goldstone is massless. The charged Higgs boson mass is also very easily determined to be

$$m_{H^\pm}^2 = Y_2 + \tfrac{1}{2}Z_3 v^2 \,. \tag{2.10}$$

The three neutral fields mix and the neutral Higgs squared-mass matrix in the φ_1^0–φ_2^0–a^0 basis becomes

$$\mathcal{M} = v^2 \begin{pmatrix} Z_1 & \mathrm{Re}(Z_6) & -\mathrm{Im}(Z_6) \\ \mathrm{Re}(Z_6) & \frac{1}{2}\left[Z_{34} + \mathrm{Re}(Z_5)\right] + Y_2/v^2 & -\frac{1}{2}\mathrm{Im}(Z_5) \\ -\mathrm{Im}(Z_6) & -\frac{1}{2}\mathrm{Im}(Z_5) & \frac{1}{2}\left[Z_{34} - \mathrm{Re}(Z_5)\right] + Y_2/v^2 \end{pmatrix}, \tag{2.11}$$

where $Z_{34} = Z_3 + Z_4$ and from complex analysis, the simplification

$$\mathrm{Im}(z) = \frac{z - \bar{z}}{2i} \qquad \mathrm{Re}(z) = \frac{z + \bar{z}}{2} \tag{2.12}$$

is implied.

$\mathcal{M}$ is not invariant because of the χ dependence of Z_5 and Z_6. However, the eigenvalues and normalized eigenvectors are invariant. This is made apparent through the following mathematical argument. By computing the characteristic equation,

$$\det(\mathcal{M} - xI) = -x^3 + \mathrm{Tr}(\mathcal{M})\, x^2 - \tfrac{1}{2}\left[(\mathrm{Tr}\mathcal{M})^2 - \mathrm{Tr}(\mathcal{M}^2)\right] x + \det(\mathcal{M})\,, \quad (2.13)$$

where I is the 3×3 identity matrix. Unpacking this equation, we see

$$\begin{aligned}
\mathrm{Tr}(\mathcal{M}) &= 2Y_2 + (Z_1 + Z_3 + Z_4)v^2\,, \\
\mathrm{Tr}(\mathcal{M}^2) &= Z_1^2 v^4 + \tfrac{1}{2}v^4\left[(Z_3 + Z_4)^2 + |Z_5|^2 + 4|Z_6|^2\right] \\
&\quad +2Y_2[Y_2 + (Z_3 + Z_4)v^2], \\
\det(\mathcal{M}) &= \tfrac{1}{4}\{Z_1 v^6[(Z_3 + Z_4)^2 - |Z_5|^2] - 2v^4[2Y_2 + (Z_3 + Z_4)v^2]|Z_6|^2 \\
&\quad +4Y_2 Z_1 v^2[Y_2 + (Z_3 + Z_4)v^2] + 2v^6 \mathrm{Re}(Z_5^* Z_6^2)\}
\end{aligned} \quad (2.14)$$

Because all of the coefficients in the mass matrix $\mathcal{M}$ are invariant, the physical Higgs masses will be basis-independent as well. It is necessary to diagonalize $\mathcal{M}$ so that only the eigenvalues lie along the diagonal and only the squared-mass terms are present. By diagonalizing the mass matrix, we are identifying the physical particles since physical particles are states of definite mass.

$$R\mathcal{M}R^T = \mathcal{M}_D \equiv \mathrm{diag}\,(m_1^2\,,\, m_2^2\,,\, m_3^2)\,, \quad (2.15)$$

where $RR^T = I$ and the m_k^2 are the eigenvalues of $\mathcal{M}$. R is expressed

$$\begin{aligned}
R &= R_{12}R_{13}R_{23} \\
&= \begin{pmatrix} c_{12} & -s_{12} & 0 \\ s_{12} & c_{12} & 0 \\ 0 & 0 & 1 \end{pmatrix} \begin{pmatrix} c_{13} & 0 & -s_{13} \\ 0 & 1 & 0 \\ s_{13} & 0 & c_{13} \end{pmatrix} \begin{pmatrix} 1 & 0 & 0 \\ 0 & c_{23} & -s_{23} \\ 0 & s_{23} & c_{23} \end{pmatrix} \\
&= \begin{pmatrix} c_{13}c_{12} & -c_{23}s_{12} - c_{12}s_{13}s_{23} & -c_{12}c_{23}s_{13} + s_{12}s_{23} \\ c_{13}s_{12} & c_{12}c_{23} - s_{12}s_{13}s_{23} & -c_{23}s_{12}s_{13} - c_{12}s_{23} \\ s_{13} & c_{13}s_{23} & c_{13}c_{23} \end{pmatrix},
\end{aligned} \quad (2.16)$$

where for the sake of simplification, $c_{ij} \equiv \cos\theta_{ij}$ and $s_{ij} \equiv \sin\theta_{ij}$.

The three new neutral Higgs mass-eigenstates are denoted h_1, h_2, h_3 such that

$$\begin{pmatrix} h_1 \\ h_2 \\ h_3 \end{pmatrix} = R \begin{pmatrix} \varphi_1^0 \\ \varphi_2^0 \\ a^0 \end{pmatrix}. \quad (2.17)$$

These are the neutral Higgs particles that would actually be observed with masses m_1, m_2, and m_3. Without loss of generality, it is convenient to order h_k such that $m_1 \leq m_2 \leq m_3$.

It is not immediately obvious that Eqn. (2.15) is invariant. The $\mathcal{M}$ mass matrix depends upon the choice of Higgs basis because of the χ dependence of

Z_5 and Z_6. However, because θ_{12} and θ_{13} (modulo π) are U(2)-invariant and $Z_5\, e^{-2i\theta_{23}}$, $Z_6\, e^{-i\theta_{23}}$ and $Z_7\, e^{-i\theta_{23}}$ are U(2)-invariant, $\mathcal{M}_D$ can be rewritten as

$$\widetilde{R}\,\widetilde{\mathcal{M}}\,\widetilde{R}^T = \mathcal{M}_D = \mathrm{diag}(m_1^2\,,\, m_2^2\,,\, m_3^2)\,, \tag{2.18}$$

where

$$\begin{aligned}\widetilde{\mathcal{M}} &\equiv R_{23}\mathcal{M}R_{23}^T \\ &= v^2\begin{pmatrix} Z_1 & \mathrm{Re}(Z_6\, e^{-i\theta_{23}}) & -\mathrm{Im}(Z_6\, e^{-i\theta_{23}}) \\ \mathrm{Re}(Z_6 e^{-i\theta_{23}}) & \mathrm{Re}(Z_5\, e^{-2i\theta_{23}}) + A^2/v^2 & -\frac{1}{2}\mathrm{Im}(Z_5\, e^{-2i\theta_{23}}) \\ -\mathrm{Im}(Z_6\, e^{-i\theta_{23}}) & -\frac{1}{2}\mathrm{Im}(Z_5\, e^{-2i\theta_{23}}) & A^2/v^2 \end{pmatrix},\end{aligned} \tag{2.19}$$

and

$$\widetilde{R} = \begin{pmatrix} c_{12}c_{13} & -s_{12} & -c_{12}s_{13} \\ c_{13}s_{12} & c_{12} & -s_{12}s_{13} \\ s_{13} & 0 & c_{13} \end{pmatrix}. \tag{2.20}$$

All terms in the $\widetilde{\mathcal{M}}$ are invariant because Eqn. (2.7) recalls that two pseudo-invariant quantities generate an invariant quantity when multiplied. Therefore,

$$\widetilde{R}\,\widetilde{\mathcal{M}}\,\widetilde{R}^T = \mathcal{M}_D = \mathrm{diag}(m_1^2\,,\, m_2^2\,,\, m_3^2)\,, \tag{2.21}$$

and $\widetilde{R}$, $\widetilde{\mathcal{M}}$, and $\widetilde{R}^T$ are invariants.

For the sake of simplicity, Table 2.1 represents the conventional substitutions for the neutral Higgs mixing angles. These angles can be thought of as

Table 2.1: The invariant quantities $q_{k\ell}$ are functions of the the neutral Higgs mixing angles θ_{12} and θ_{13}, where $c_{ij} \equiv \cos\theta_{ij}$ and $s_{ij} \equiv \sin\theta_{ij}$ taken from reference [1].

k	q_{k1}	q_{k2}
1	$c_{12}c_{13}$	$-s_{12} - ic_{12}s_{13}$
2	$s_{12}c_{13}$	$c_{12} - is_{12}s_{13}$
3	s_{13}	ic_{13}
4	i	0

representing the pseudo-invariant nature of the generic 2HDM within a specific and invariant model. As will be shown, the invariant angles $q_{k\ell}$ are used to write expressions for physical quantities in basis-independent form.

Chapter 3

Phenomenology of the 2HDM

3.1 The Oblique Parameters

The basis-independent Two-Higgs Doublet Model has implications for the values of many experimental parameters. The Large Hadron Collider is optimized to make discoveries at the electroweak scale and should provide experimental evidence for the existence or non-existance of the Higgs particle. As the LHC has become operational again as of the 20th of November 2009, refining experimental predictions and constraints for the 2HDM is a pressing research goal. For this purpose the "Oblique Parameters," S, T, U, V, W, and X are experimentally accessible values which can constrain or disprove a theory. The 2HDM predicts values for the oblique parameters which may or may not be compatible with those measured experimentally.

The S, T, U, V, W, and X parameters are the link between theory and experiment. Experimentally, these parameters can be determined only indirectly through the determination of constants such as m_z, m_w, and decay rates. Burgess and London [6] have defined these parameters such that

$$\frac{\alpha S}{4s_w^2 4c_w^2} = \left[\frac{\delta\Pi_{ZZ}(M_Z^2) - \delta\Pi_{ZZ}(0)}{M_Z^2}\right] - \frac{(c_w^2 - s_w^2)}{s_w c_w}\delta\Pi'_{Z\gamma}(0) - \delta\Pi'_{\gamma\gamma}(0), \tag{3.1}$$

$$\alpha T = \frac{\delta\Pi_{WW}(0)}{M_W^2} - \frac{\delta\Pi_{ZZ}(0)}{M_Z^2}, \tag{3.2}$$

$$\frac{\alpha U}{4s_w^2} = \left[\frac{\delta\Pi_{WW}(M_W^2) - \delta\Pi_{WW}(0)}{M_W^2}\right] - c_w^2\left[\frac{\delta\Pi_{ZZ}(M_Z^2) - \delta\Pi_{ZZ}(0)}{M_Z^2}\right] - s_w^2\delta\Pi'_{\gamma\gamma}(0) - 2s_w c_w\delta\Pi'_{Z\gamma}(0). \tag{3.3}$$

Additionally,

$$\alpha V = \delta\Pi'_{ZZ}(M_Z^2) - \left[\frac{\delta\Pi_{ZZ}(M_Z^2) - \delta\Pi_{ZZ}(0)}{M_Z^2}\right], \tag{3.4}$$

$$\alpha W = \delta\Pi'_{WW}(M_W^2) - \left[\frac{\delta\Pi_{WW}(M_W^2) - \delta\Pi_{WW}(0)}{M_W^2}\right], \tag{3.5}$$

$$\alpha X = -s_w c_w \left[\frac{\delta\Pi_{Z\gamma}(M_Z^2)}{M_Z^2} - \delta\Pi'_{Z\gamma}(0)\right]. \tag{3.6}$$

The parameters α, s_w, c_w are constants and are defined in section 3.2.1. The vacuum polarization tensors Π_{ij} are functions calculated using the Feynman rules corresponding to possible vertices of the 2HDM. These are derived and displayed in [3].

3.2 Analytical

This section represents original results. The derivations for Eqns. 3.16-3.31 were determined using Mathematica or drawn from integral tables.

To produce numerical results, it is necessary to evaluate $B_{22}(q^2; m_1^2; m_2^2)$, $B_0(q^2; m_1^2; m_2^2)$, and $A_0(q^2; m_1^2; m_2^2)$ functions which appear in Eqns. 3.52-3.60. The functions B_{22} and B_0 are defined in ref. [4] and come from the evaluation of two-point integrals. They can be evaluated using the following formulae of ref. [2]:

$$B_{22}(q^2; m_1^2, m_2^2) = \frac{1}{4}(\Delta + 1)[m_1^2 + m_2^2 - \frac{1}{3}q^2] - \tfrac{1}{2}\int_0^1 dx X \ln(X - i\epsilon), \tag{3.7}$$

$$B_0(q^2; m_1^2, m_2^2) = \Delta - \int_0^1 dx \ln(X - i\epsilon)\,, \tag{3.8}$$

$$A_0(m^2) = m^2(\Delta + 1 - \ln m^2)\,, \tag{3.9}$$

where $X \equiv m_1^2 x + m_2^2(1-x) - q^2 x(1-x)$ and $\Delta \equiv \frac{2}{4-d} + \ln(4\pi) - \gamma$, in d space-time dimensions. These equations are evaluated as the limit $\epsilon \to 0$ and $d \to 4$. As $d \to 4$, there are apparent infinities which arise in the first terms of Eqns. 3.7-3.9. However, when explicitly adding the Feynman diagrams which contribute to each vacuum polarization tensor Π_{ij} of Eqns. 3.1-3.6, it was found that these infinities annihilate. In practice, with the additional constraint that $\epsilon \to 0$, Eqns. 3.7-3.9 become

$$B_{22}(q^2;m_1^2,m_2^2) = -\tfrac{1}{2}\int_0^1 dx\big(m_1^2x+m_2^2(1-x)-q^2x(1-x)\big)\ln\big[m_1^2x +m_2^2(1-x)-q^2x(1-x)\big], \quad (3.10)$$

$$B_0(q^2;m_1^2,m_2^2) = \int_0^1 dx\ln\left[m_1^2x+m_2^2(1-x)-q^2x(1-x)\right], \quad (3.11)$$

$$A_0(m^2) = m^2(-\ln m^2). \quad (3.12)$$

Expanding these integrals turns Eqns. 3.10 and 3.11 into a linear combination of three distinct integrals namely:

$$F_0[q^2,m_1^2,m_2^2] = \int_0^1 \ln(q^2x^2+m_1^2x+m_2^2)dx, \quad (3.13)$$

$$F_1[q^2,m_1^2,m_2^2] = \int_0^1 x\ln(q^2x^2+m_1^2x+m_2^2)dx, \quad (3.14)$$

$$F_2[q^2,m_1^2,m_2^2] = \int_0^1 x^2\ln(q^2x^2+m_1^2x+m_2^2)dx, \quad (3.15)$$

which evaluate to

$$F_0[a,b,c] = \ln(a+b+c)+\frac{1}{2a}\left(-4a+b\ln\left(\frac{a+b+c}{c}\right) +4(ac-b^2)G_0[a,b,c]\right), \quad (3.16)$$

$$F_1[a,b,c] = \frac{1}{4a^2}\left(2a^2\ln(a+b+c)-2a^2+2ba +(2ac-b^2)\ln\left(\frac{a+b+c}{c}\right) +b(b^2-4ac)G_0[a,b,c]\right), \quad (3.17)$$

$$F_2[a,b,c] = \frac{1}{3}\left(\ln(a+b+c)-\frac{2}{3}+\frac{b}{2a}-\frac{b^2-2ac}{a^2} +\frac{b}{2a^3}(b^2-3ac)\ln\left(\frac{a+b+c}{c}\right) +\frac{c}{2a^2}\left(5b^2-4ac-\frac{b^4}{ac}\right)G_0[a,b,c]\right), \quad (3.18)$$

where $G_0[a,b,c]$ varies such that

$$\begin{aligned} G_0[a,b,c] &= \frac{2}{\sqrt{4ac-b^2}}\left[\arctan\left(\frac{2a+b}{\sqrt{4ac-b^2}}\right)\right. \\ &\quad \left. -\arctan\left(\frac{b}{\sqrt{4ac-b^2}}\right)\right] \text{ if } b^2<4ac, \end{aligned} \tag{3.19}$$

$$G_0[a,b,c] = \left(\frac{-2}{2a+b+\frac{2}{b}}\right) \text{ if } b^2=4ac, \tag{3.20}$$

$$G_0[a,b,c] = \frac{1}{\sqrt{-4ac+b^2}}\ln\left(\frac{b+2c+\sqrt{-4ac+b^2}}{b+2c-\sqrt{-4ac+b^2}}\right) \text{ if } b^2>4ac. \tag{3.21}$$

However, in cases where $a=0$, we need three additional integrals:

$$\begin{aligned} F_{00} &= -1-\frac{c\ln(c)}{b}+\ln(b+c)+\frac{c\ln(b+c)}{b} \text{ if } b\neq c, \\ & F_{00} = -1+\ln(2)+\ln(2c) \text{ if } b=c, \end{aligned} \tag{3.22}$$

$$F_{10} = \frac{-1}{4}+\frac{c}{2b}+\frac{c^2\ln(c)}{2b^2}+\frac{1}{2}\ln(b+c)-\frac{c^2\ln(b+c)}{2b^2}, \tag{3.23}$$

$$F_{20} = \frac{-1}{9}+\frac{c}{6b}-\frac{c^2}{3b^2}-\frac{c^3\ln(c)}{3b^3}+\frac{\ln(b+c)}{3}+\frac{c^3\ln(b+c)}{3b^3}. \tag{3.24}$$

Using these functions it is now possible to define Eqns. 3.10-3.11

$$\begin{aligned} B_{22}[a,b,c] &= \frac{-1}{2}\Big(aF_2[a,b-a-c,c]+(b-c-a)F_1[a,b-a-c,c] \\ &\quad +cF_0[a,b-a-c,c]\Big), \end{aligned} \tag{3.25}$$

$$B_0[a,b,c] = -F_0[a,b-a-c,c]. \tag{3.26}$$

The substitution "b" $= b-a-c$ into Eqns. 3.16-3.18 is a result of the fact that

$$\begin{aligned} X &= m_1^2x+m_2^2(1-x)-q^2x(1-x) \\ &= m_2^2+(m_1^2-q^2-m_2^2)x+q^2x^2 \end{aligned} \tag{3.27}$$

For the cases when $q^2=0$, Eqn. 3.10 remains the same if $b=c$. However, when $b\neq c$

$$B_{22}[a,b,c] = \frac{A_0[c]}{2}. \tag{3.28}$$

In addition, for all values of b and c

$$B_0[a,b,c] = \frac{A_0[b]-A_0[c]}{b-c}. \tag{3.29}$$

It is also necessary to define the derivative $\frac{\partial B_{22}[a,b,c]}{c} = B'_{22}[a,b,c]$ and $\frac{\partial B_0[a,b,c]}{\partial a} = B'_0[a,b,c]$. These partial derivatives are complicated when $a\neq 0$. However, when $a=0$,

$$B'_{22}[0,b,c] = -\frac{1}{72(b-c)^3}\Big[-b^3-9b^2c+9bc^2+c^3-6b^2(b-3c)\ln(b) +(6c^3-18bc^2)\ln(c)\Big] \text{ if } b\neq c \quad (3.30)$$

$$B'_{22}[0,b,c] = \frac{1}{12}[1+\ln(c)] \text{ if } b=c. \quad (3.31)$$

The $B'_0[a,b,c]$ function is not necessary for $a=0$.

3.2.1 Constants

To use the above functions, it is also necessary to define constants. Constants were derived in such a manner that their definition depended solely on the most precise observable quantities available. These fundamental constants are

$$G_F = 1.16637\times10^{-5}\text{GeV}^{-2}, \quad (3.32)$$

$$M_Z = 91.1876\text{GeV}, \quad (3.33)$$

$$\alpha = \frac{1}{137.035999}, \quad (3.34)$$

where G_F is Fermi's coupling constant, M_Z is the mass of the Z-boson, and α is the dimensionless fine structure constant. Using these observable quantities, it is possible to derive the remainder of the constants necessary for our analysis. The weak mixing angle θ_W was derived using the equation:

$$\cos(\theta_W)^2\sin(\theta_W)^2 = \alpha\pi\frac{\sqrt{2}}{2G_FM_Z^2}. \quad (3.35)$$

The derived value for θ_W was 0.48673. In order for the Higgs mechanism to work, the Higgs field requires a non-zero vacuum expectation value. The vacuum expectation value v for the Higgs field is derived:

$$\nu = (\sqrt{2}G_F)^{-\frac{1}{2}} = 246\text{GeV}. \quad (3.36)$$

The gauge coupling parameter g is derived:

$$g = \frac{\sqrt{4\pi\alpha}}{\sin(\theta_W)} = 0.657449, \quad (3.37)$$

and is by nature dimensionless. Using the value of θ_W, one determines that:

$$c_W = 0.887607 \quad (3.38)$$

$$s_W = 0.460602. \quad (3.39)$$

The constants c_{2W} and s_{2W} are defined using the identities

$$c_{2W} \equiv c_W^2 - s_W^2, \tag{3.40}$$
$$s_{2W} \equiv 2 s_W c_W. \tag{3.41}$$

Lastly, the mass of the W-boson $W^{\pm}$ was determined using the equation:

$$M_W = \cos(\theta_W) M_Z. \tag{3.42}$$

3.2.2 Defining m_i

Because the values for m_1, m_2, m_3, and $m_{H^{\pm}}$ have not yet been observed experimentally, it is necessary to arbitrarily vary the constants in the matrix of Eqn. 2.11. The values of Z_1, $\mathrm{Re}(Z_6 e^{-i\theta_{23}})$, $\mathrm{Im}(Z_6 e^{-i\theta_{23}})$, $\mathrm{Re}(Z_5 e^{-2i\theta_{23}})$, $\mathrm{Im}(Z_5 e^{-2i\theta_{23}})$, $Z_{34} = Z_3 + Z_4$, and Z_3 were arbitrarily varied according to Table 3.1.

Table 3.1: The theoretical limits of the parameters Z_1, $\mathrm{Re}(Z_6 e^{-i\theta_{23}})$, $\mathrm{Im}(Z_6 e^{-i\theta_{23}})$, $\mathrm{Re}(Z_5 e^{-2i\theta_{23}})$, $\mathrm{Im}(Z_5 e^{-2i\theta_{23}})$, $Z_{34} = Z_3 + Z_4$, and Z_3. These values were varied arbitrarily to produce values for m_1, m_2, m_3, and $m_{H^{\pm}}$. The values for these theoretical upper bounds were found in [3].

Theoretical Upper Bound
$\lvert Z_1 \rvert < 4\pi$
$\lvert Z_3 \rvert < 8\pi$
$\lvert Z_3 + Z_4 \rvert < 8\pi$
$\lvert \mathrm{Re}(Z_5 e^{-2i\theta_{23}}) \rvert < 2\pi$
$\lvert \mathrm{Re}(Z_6 e^{-i\theta_{23}}) \rvert < 2\pi$
$\lvert \mathrm{Im}(Z_5 e^{-2i\theta_{23}}) \rvert < 2\pi$
$\lvert \mathrm{Im}(Z_6 e^{-i\theta_{23}}) \rvert < 2\pi$

Using Eqn. 2.15, the mass of m_1, m_2, m_3 can be determined, with the results

$$m_1 = \sqrt{\nu^2 \lambda_1}, \tag{3.43}$$
$$m_2 = \sqrt{\nu^2 \lambda_2}, \tag{3.44}$$
$$m_3 = \sqrt{\nu^2 \lambda_3}, \tag{3.45}$$

where λ_1, λ_2, λ_3, are the eigenvalues of the mass matrix from Eqn. 2.15, ordered such that $\lambda_1 < \lambda_2 < \lambda_3$. The charged Higgs mass, $m_{H^{\pm}}$ can be determined using Eqn. 2.10.

From [1], the invariant quantities q_{kl} as displayed in Table 2.1 can be determined using the equations:

$$q_{11}^2 = 1 - q_{21}^2 - q_{31}^2, \tag{3.46}$$

$$q_{21}^2 = \frac{(Z_1\nu^2 - m_1^2)(Z_1\nu^2 - m_2^2) - (\mathrm{Im}(Z_6)^2 + \mathrm{Re}(Z_6)^2)\nu^4}{(m_2^2 - m_1^2)(m_3^2 - m_2^2)}, \tag{3.47}$$

$$q_{31}^2 = \frac{(Z_1\nu^2 - m_1^2)(m_3^2 - Z_1\nu^2) - (\mathrm{Im}(Z_6)^2 + \mathrm{Re}(Z_6)^2)\nu^4}{(m_3^2 - m_1^2)(m_3^2 - m_2^2)}, \tag{3.48}$$

and

$$q_{12}^2 = q_{31}^2 + q_{21}^2, \tag{3.49}$$

$$q_{22}^2 = q_{11}^2 + q_{31}^2, \tag{3.50}$$

$$q_{32}^2 = 1 - q_{31}^2. \tag{3.51}$$

3.2.3 The Vacuum Polarization Tensors

Having defined the necessary constants and variables as well as all possible cases for Eqns. 3.7-3.9, the last necessary step is to explicitly define numerical values for the vacuum polarization tensors $\delta\Pi_{ij}(a)$ from Eqns. 3.1-3.6. They are defined:

$$\begin{aligned}
\delta\Pi_{ZZ}(M_Z^2) = \frac{\alpha}{4\pi s_w^2}\Big\{ & - m_Z^2\big(q_{11}^2 B_0[m_Z^2, m_Z^2, m_1^2] + q_{21}^2 B_0[m_Z^2, m_Z^2, m_2^2] \\
& + q_{31}^2 B_0[m_Z^2, m_Z^2, m_3^2]\big) + q_{11}^2 B_{22}[m_Z^2, m_Z^2, m_1^2] \\
& + q_{21}^2 B_{22}[m_Z^2, m_Z^2, m_2^2] + q_{31}^2 B_{22}[m_Z^2, m_Z^2, m_3^2] \\
& + q_{21}^2 B_{22}[m_Z^2, m_1^2, m_3^2] + q_{11}^2 B_{22}[m_Z^2, m_2^2, m_3^2] \\
& + q_{31}^2 B_{22}[m_Z^2, m_1^2, m_2^2] + c_{2w}^2 B_{22}[m_Z^2, m_{H^\pm}^2, m_{H^\pm}^2] \\
& - \frac{1}{2}\big(A_0[m_1^2] + A_0[m_2^2] + A_0[m_3^2]\big) \\
& \text{(Standard Model Contribution)} \\
& - \big(- m_Z^2 B_0[m_Z^2, m_Z^2, m_1^2] + B_{22}[m_Z^2, m_Z^2, m_1^2]\big)\Big\},
\end{aligned} \tag{3.52}$$

$$
\begin{aligned}
\delta\Pi_{ZZ}(0) \;=\; & \frac{\alpha}{4\pi c_w^2 s_w^2}\Bigg\{ - m_Z^2\big(q_{11}^2 B_0[0,m_Z^2,m_1^2] + q_{21}^2 B_0[0,m_Z^2,m_2^2] \\
& + q_{31}^2 B_0[0,m_Z^2,m_3^2] + q_{11}^2 B_{22}[0,m_Z^2,m_1^2] + q_{21}^2 B_{22}[0,m_Z^2,m_2^2] \\
& + q_{31}^2 B_{22}[0,m_Z^2,m_3^2] + q_{21}^2 B_{22}[0,m_1^2,m_3^2] + q_{11}^2 B_{22}[0,m_2^2,m_3^2] \\
& + q_{31}^2 B_{22}[0,m_1^2,m_2^2] \\
& - \frac{1}{2}\big(A_0[m_1^2] + A_0[m_2^2] + A_0[m_3^2] + A_0[m_{H^\pm}^2] - c_{2w}^2 A_0[m_{H^\pm}^2]\big) \\
& \text{(Standard Model Contribution)} \\
& - \big(- m_Z^2 B_0[0,m_Z^2,m_1^2] + B_{22}[0,m_Z^2,m_1^2]\big)\Bigg\}, \qquad (3.53)
\end{aligned}
$$

$$
\begin{aligned}
\delta\Pi'_{ZZ}(M_Z^2) \;=\; & \frac{\alpha}{4\pi c_w^2 s_w^2}\Bigg\{ - m_Z^2\big(q_{11}^2 B_0'[m_Z^2,m_Z^2,m_1^2] + q_{21}^2 B_0'[m_Z^2,m_Z^2,m_2^2] \\
& + q_{31}^2 B_0'[m_Z^2,m_Z^2,m_3^2]) + q_{11}^2 B_{22}'[m_Z^2,m_Z^2,m_1^2] \\
& + q_{21}^2 B_{22}'[m_Z^2,m_Z^2,m_2^2] + q_{21}^2 B_{22}'[m_Z^2,m_1^2,m_3^2] \\
& + q_{11}^2 B_{22}'[m_Z^2,m_2^2,m_3^2] + q_{31}^2 B_{22}'[m_Z^2,m_1^2,m_2^2] \\
& + q_{31}^2 B_{22}'[m_Z^2,m_Z^2,m_3^2] + c_{2w}^2 B_{22}'[m_Z^2,m_{H^\pm}^2,m_{H^\pm}^2] \\
& \text{(Standard Model Contribution)} \\
& - (-m_Z^2 B_0'[m_Z^2,m_Z^2,m_1^2] + B_{22}'[m_Z^2,m_Z^2,m_1^2])\Bigg\}, \qquad (3.54)
\end{aligned}
$$

$$
\begin{aligned}
\delta\Pi_{WW}(m_W^2) \;=\; & \frac{\alpha}{4\pi s_w^2}\Bigg\{ - m_W^2\big(q_{11}^2 B_0[m_W^2,m_W^2,m_1^2] + q_{21}^2 B_0[m_W^2,m_W^2,m_2^2] \\
& + q_{31}^2 B_0[m_W^2,m_W^2,m_3^2]) + q_{11}^2 B_{22}[m_W^2,m_W^2,m_1^2] \\
& + q_{21}^2 B_{22}[m_W^2,m_W^2,m_2^2] + q_{31}^2 B_{22}[m_W^2,m_W^2,m_3^2] \\
& + q_{21}^2 B_{22}[m_W^2,m_1^2,m_3^2] + q_{11}^2 B_{22}[m_W^2,m_2^2,m_3^2] \\
& + q_{31}^2 B_{22}[m_W^2,m_1^2,m_2^2] + c_{2w}^2 B_{22}[m_W^2,m_{H^\pm}^2,m_{H^\pm}^2] \\
& - \frac{1}{2}\big(A_0[m_1^2] + A_0[m_2^2] + A_0[m_3^2]\big) \\
& \text{(Standard Model Contribution)} \\
& - (-m_W^2 B_0[m_W^2,m_W^2,m_1^2] + B_{22}[m_W^2,m_W^2,m_1^2])\Bigg\}, \qquad (3.55)
\end{aligned}
$$

$$\begin{aligned}\delta\Pi_{WW}(0) &= \frac{\alpha}{4\pi s_w^2}\Big\{ - m_Z^2\big(q_{11}^2 B_0[0,m_W^2,m_1^2] + q_{21}^2 B_0[0,m_W^2,m_2^2] \\ &+q_{31}^2 B_0[0,m_W^2,m_3^2]\big) + q_{11}^2 B_{22}[0,m_W^2,m_1^2] \\ &+q_{21}^2 B_{22}[0,m_W^2,m_2^2] + q_{12}^2 B_{22}[0,m_{H^\pm}^2,m_1^2] \\ &+q_{22}^2 B_{22}[0,m_{H^\pm}^2,m_2^2] + q_{32}^2 B_{22}[0,m_{H^\pm}^2,m_3^2] \\ &+q_{31}^2 B_{22}[0,m_W^2,m_3^2] \\ &-\frac{1}{2}\big(A_0[m_1^2] + A_0[m_2^2] + A_0[m_3^2] + A_0[m_{H^\pm}^2]\big) \\ &\text{(Standard Model Contribution)} \\ &-\big(- m_W^2 B_0[0,m_Z^2,m_1^2] + B_{22}[0,m_W^2,m_1^2]\big)\Big\}, \end{aligned} \tag{3.56}$$

$$\begin{aligned}\delta\Pi'_{WW}(M_W^2) &= \frac{\alpha}{4\pi s_w^2}\Big\{ m_W^2\big(q_{11}^2 B_0'[m_W^2,m_W^2,m_1^2] + q_{21}^2 B_0'[m_W^2,m_W^2,m_2^2] \\ &+q_{31}^2 B_0'[m_W^2,m_W^2,m_3^2]\big) + q_{11}^2 B_{22}'[m_W^2,m_W^2,m_1^2] \\ &+q_{21}^2 B_{22}'[m_W^2,m_W^2,m_2^2] + q_{31}^2 B_{22}'[m_W^2,m_W^2,m_3^2] \\ &+q_{12}^2 B_{22}'[m_W^2,m_W^2,m_1^2] + q_{22}^2 B_{22}'[m_W^2,m_W^2,m_2^2] \\ &+q_{32}^2 B_{22}'[m_W^2,m_W^2,m_3^2] \\ &\text{Standard Model Contribution} \\ &-\big(- m_W^2 B_0'[0,m_Z^2,m_1^2] + B_{22}'[0,m_W^2,m_1^2]\big)\Big\}, \end{aligned} \tag{3.57}$$

$$\begin{aligned}\delta\Pi_{Z\gamma}(m_Z^2) &= \frac{\alpha}{2\pi s_w^2}\Big(\frac{c_{2w}^2}{c_w^2}\big(B_{22}[m_Z^2,m_{H^\pm}^2,m_{H^\pm}^2] \\ &\qquad - B_{22}[0,m_{H^\pm}^2,m_{H^\pm}^2]\big)\Big), \end{aligned} \tag{3.58}$$

$$\delta\Pi'_{Z\gamma}(0) = \frac{\alpha}{\pi}\big(B_{22}'[0,m_{H^\pm}^2,m_{H^\pm}^2]\big), \tag{3.59}$$

$$\delta\Pi'_{\gamma\gamma}(0) = \frac{\alpha}{2\pi s_w^2}\big(B_{22}'[0,m_{H^\pm}^2,m_{H^\pm}^2]\big). \tag{3.60}$$

Eqs. 3.52-3.60 produce real-valued numerical results for varying values of $m_{1,2,3,H^\pm}$.

These numerical results exhibit relationships between the six oblique parameters (S, T, U, V, W, and X) and $m_{1,2,3,H^\pm}$ some of which display correlation. The relationship of the oblique parameters and m_2,m_3,$m_{H\pm}$ to m_1 is especially interesting because m_1 is the mass of the lightest neutral Higgs particle and therefore the most likely to be observed in the LHC.

Chapter 4

Numerical Analysis

4.1 Generating Numerical Data

To produce values for $m_{1,2,3,H^\pm}$, and therefore the oblique parameters, the seven theoretical parameters Z_1, $\mathrm{Re}(Z_6 e^{-i\theta_{23}})$, $\mathrm{Im}(Z_6 e^{-i\theta_{23}})$, $\mathrm{Re}(Z_5 e^{-2i\theta_{23}})$, $\mathrm{Im}(Z_5 e^{-2i\theta_{23}})$, $Z_{34} = Z_3 + Z_4$, and Z_3 must be varied arbitrarily between certain theoretical boundaries. These boundaries are suggested by elements of the theory and displayed in Table 3.1. Because their particular values are not yet known, randomness is essential and every value between the boundaries must be equally probable. The effect of increasing or decreasing these limits uniformly are discussed in sections 4.3.1 and 4.3.2.

Using Mathematica, values of Z_1, $\mathrm{Re}(Z_6 e^{-i\theta_{23}})$, $\mathrm{Im}(Z_6 e^{-i\theta_{23}})$, $\mathrm{Re}(Z_5 e^{-2i\theta_{23}})$, $\mathrm{Im}(Z_5 e^{-2i\theta_{23}})$, Z_{34}, and Z_3 were varied arbitrarily according to Table 3.1. The value of Y_2 was chosen such that $Y_2 = 50$ GeV^2. Although the value of Y_2 is also unknown, this particular value for Y_2 was chosen to be consistent with [3].

Some values for Z_1, $\mathrm{Re}(Z_6 e^{-i\theta_{23}})$, $\mathrm{Im}(Z_6 e^{-i\theta_{23}})$, $\mathrm{Re}(Z_5 e^{-2i\theta_{23}})$, $\mathrm{Im}(Z_5 e^{-2i\theta_{23}})$, Z_{34}, and Z_3 produced imaginary values for m_1, m_2, m_3, $m_{H^\pm}$, V and W. These results were discarded because they are not physical. In addition, values with $m_{H^\pm} \leq 50$ GeV or $m_1 \leq 10$ GeV were discarded because they are unrealistically small. Therefore data sets of the form $\{m_1, m_2, m_3, m_{H^\pm}, S, T, U, V, W, X\}$ were kept only if

$$\mathrm{Im}(m_1) = \mathrm{Im}(m_2) = \mathrm{Im}(m_3) = \mathrm{Im}(m_{H^\pm}) = 0, \tag{4.1}$$

$$m_{H^\pm} \leq 50 \text{ GeV, and} \tag{4.2}$$

$$m_1 \leq 10 \text{ GeV}. \tag{4.3}$$

Using these constraints collectively, out of $10,000$ potential data sets of the form $\{m_1, m_2, m_3, m_{H^\pm}, S, T, U, V, W, X\}$, one typically produces ≈ 620 realistic results.

4.2 Correlations

4.2.1 Correlations Between the Oblique Parameters

The oblique parameters are related to observables that can be determined without actually observing a Higgs particle. The 2HDM predicts particular values for these oblique parameters. If these theoretical values were found to correspond to experimental values, the 2HDM would be valid.

To analyze the oblique parameters, results were displayed in 2D and 3D plots using the Mathematica 'ListPlot' function with the automatic plot-range. Although many parameters were not correlated, some displayed correlation. All of the uncorrelated group had a high density of points near the origin. For the parameters which displayed correlation, the terms 'Mild,' 'Strong,' and 'Direct' have been used to categorize the level of correlation. This categorization depends upon the parameter space as displayed by Mathematica using the automatic plot-range. The most difficult cases to categorize were between 'no correlation' and 'mild correlation.' In these cases, the entire plot-range was analyzed. My categorization was verified and concurrent with that of my advisor on the basis of visual appearance of the parameter space. 'Direct' for the purposes of this experiment means minimal spread. The results for the categorization of the oblique parameters are displayed in Table 4.1.

Table 4.1: The levels of correlation for comparisons of oblique parameters. Figs. 4.1-4.10 display these levels of correlations.

Correlation Level	Parameters
None	V-T, W-T, X-T, V-U, W-U, X-V, X-W
Mild	T-S, U-S, V-S, W-S, X-S, X-T, X-U
Strong	U-T
Direct	W-V

All parameters which exhibited correlations are displayed in Figs 4.2-4.10, except for W because of its direct correlation with V (see Fig. 4.10). The plots for these figures display the same set of 1233 data points. An example of two uncorrelated parameters is displayed in Fig. 4.1. Notice the clustering near to the origin.

The parameters which displayed a 'mild correlation' are displayed in Figs. 4.2-4.7. 'Mild' is a qualitative assessment used to categorize the correlation levels between the oblique parameters. As used presently, 'mild correlation' is one degree above 'no correlation' and one degree below 'strong correlation.'

The parameters which displayed a 'strong correlation' are displayed in Fig. 4.9. These two sets of parameters where the only set to be categorized as displaying a strong correlation. As a qualitative assessment, 'strong correlation' is one degree above 'mild correlation', and one degree below 'direct correlation'.

The parameters which displayed a 'direct correlation' are displayed in Fig. 4.10. These two parameters were the only set to be categorized as displaying

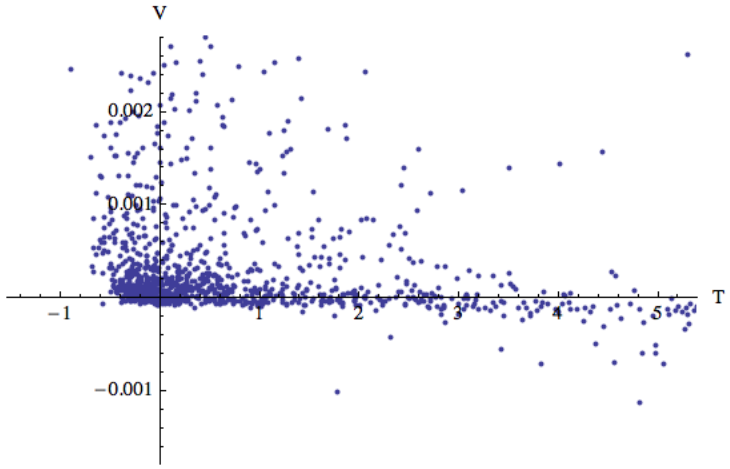

Figure 4.1: A plot of values generated for V and T. There is not a correlation between these two parameters, yet there is a clustering of values near to the origin. Other parameters without correlations include W-T, X-T, V-U, W-U, X-V, and X-W. Because of the direct correlation of V and W, the plot for W and T is very similar.

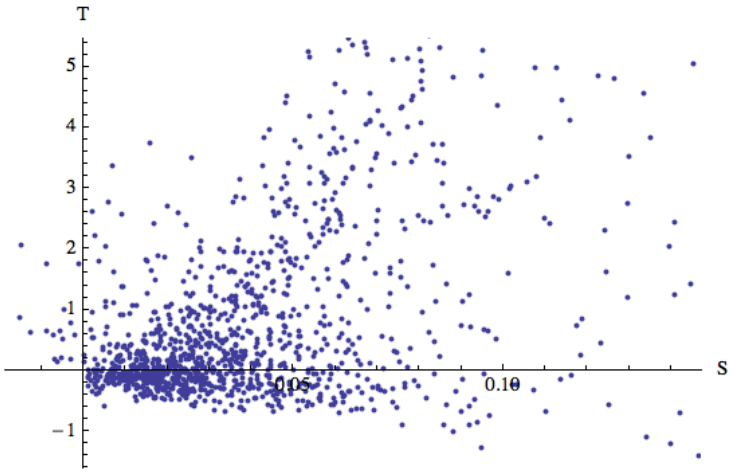

Figure 4.2: A plot of values generated for T and S. There is a mild correlation between these two parameters.

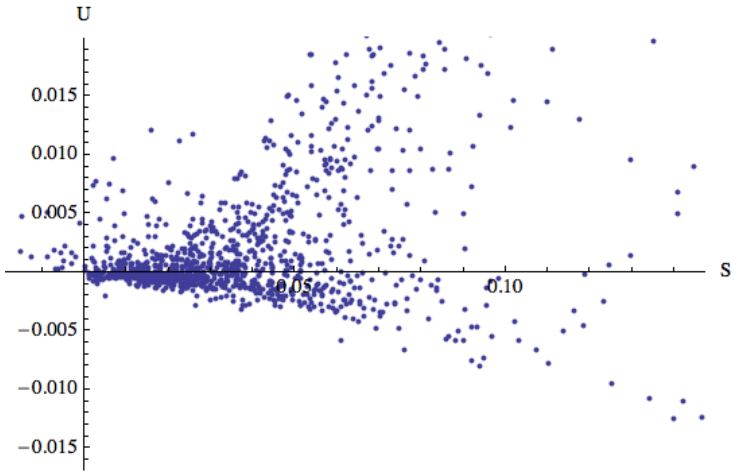

Figure 4.3: A plot of values generated for U and S. There is a mild correlation between these two parameters.

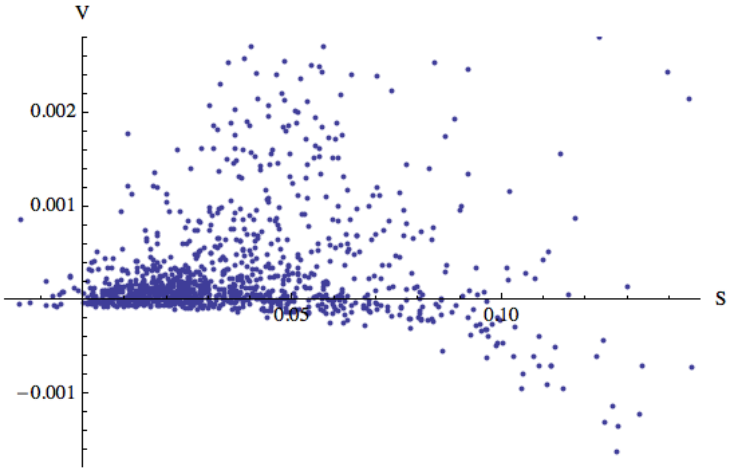

Figure 4.4: A plot of values generated for V and S. There is a mild correlation between these two parameters. This plot is very similar to W and S because there is a direct correlation between V and W (see Fig. 4.10).

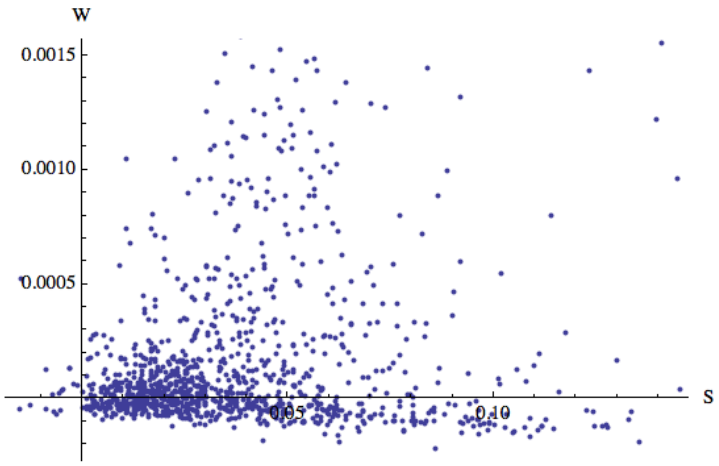

Figure 4.5: A plot of values generated for W and S. Although there may not appear to be a correlation between these parameters, adjusting the plot range to display the full set of values reveals a clearer correlation between the two parameters.

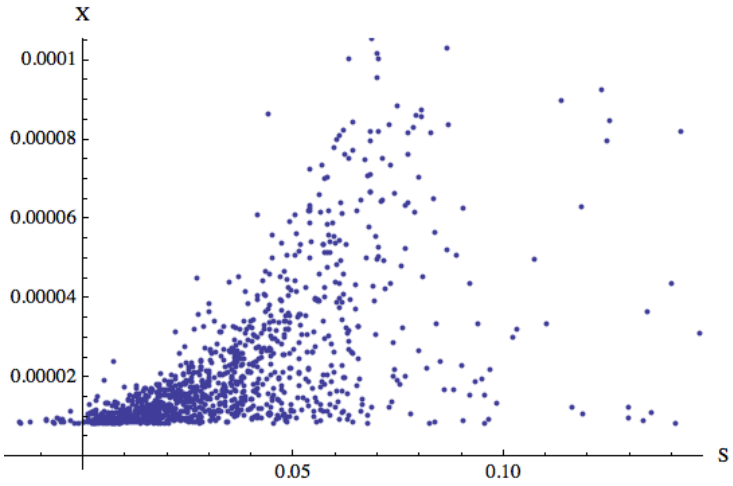

Figure 4.6: A plot of values generated for X and S. There is a mild correlation between these two parameters.

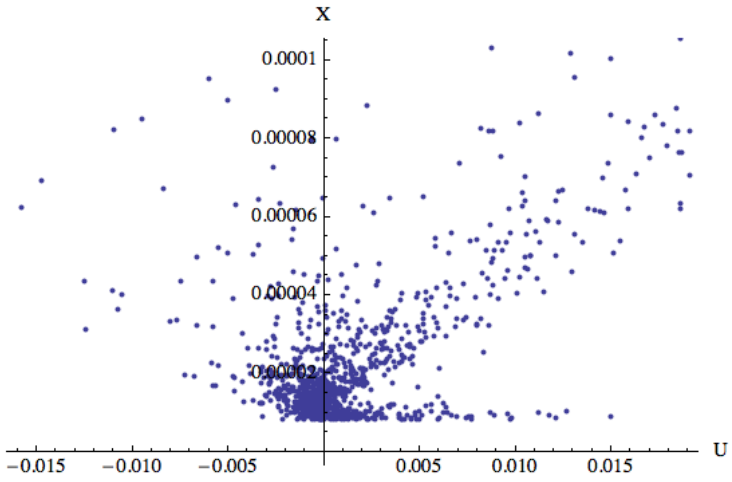

Figure 4.7: A plot of values generated for X and U. There is a mild correlation between these two parameters.

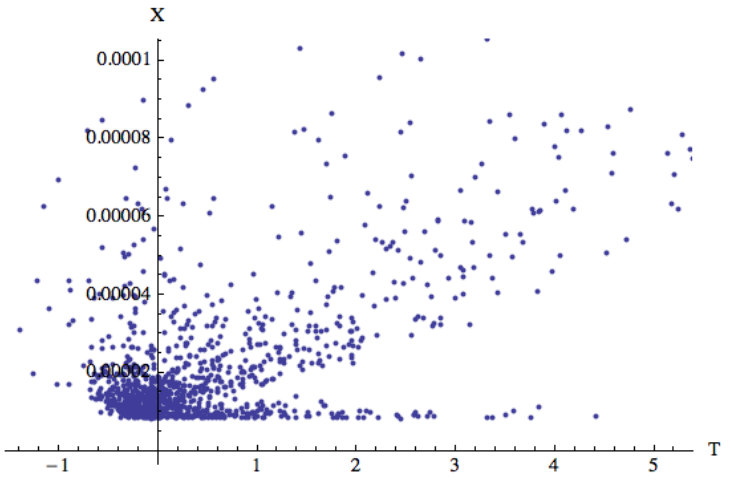

Figure 4.8: A plot of values generated for X and T. There is a mild correlation between these two parameters.

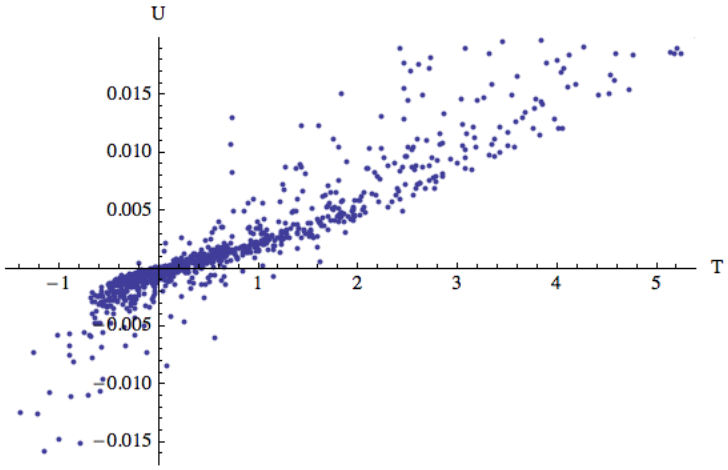

Figure 4.9: A plot of values generated for U and T. There is a strong correlation between these two parameters. No other parameters displayed this degree of correlation.

a direct correlation. As a qualitative assessment, 'direct correlation' is the strongest correlation. It is one degree above 'strong correlation.'

4.2.2 Correlation of the Oblique Parameters and m_1

After establishing the degree to which oblique parameters displayed correlations, the oblique parameters were compared to the least Higgs mass m_1. Using the theoretical limits from Table 3.1, nine two-dimensional scatter plots with 1200 data points were created displaying S, T, U, V, W, X, m_2, m_3, and $m_{H^\pm}$ with m_1. As in section 4.2.1, these plots can be categorized into levels of correlation. In this section, there are two levels of correlation, 'Mild' and 'Strong'. No 'direct correlation' was observed. A list of which parameters displayed correlation is given in Table 4.2.

Table 4.2: The levels of correlation for comparisons of m_1 with $m_{2,3,H^\pm}$ and the oblique parameters. Figs. 4.11-4.13 display these levels of correlations

Correlation Level	Parameters
None	T, X, m_2, m_3, $m_{H^\pm}$
Mild	S, U
Strong	V, W

The parameters which displayed mild correlation are displayed in Figs. 4.11 and 4.12.

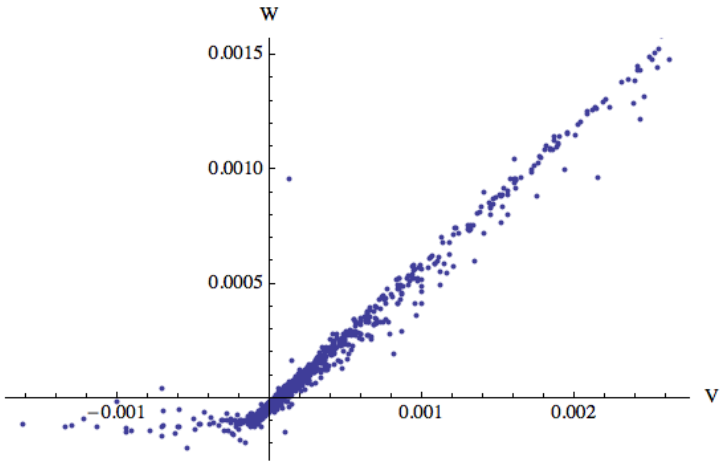

Figure 4.10: A plot of values generated for W and V. There is a direct correlation between these two parameters. No other parameters displayed this degree of correlation.

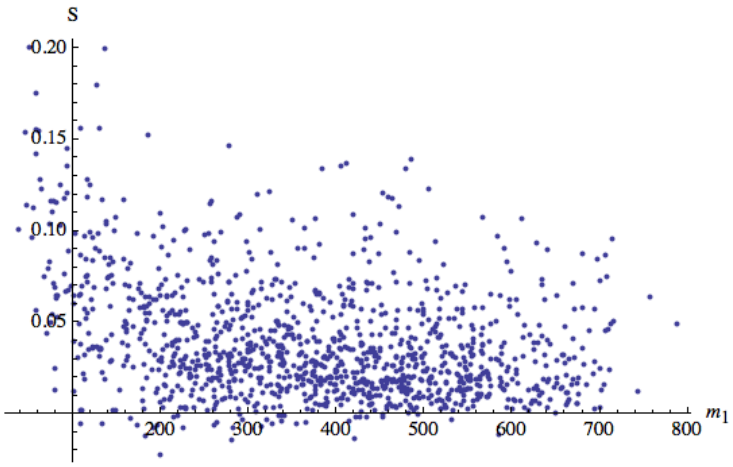

Figure 4.11: A plot of values generated for S and m_1. As m_1 increases, values for S generally decrease. Analyzing the entire range of values makes this relationship more clear. These parameters display a mild correlation.

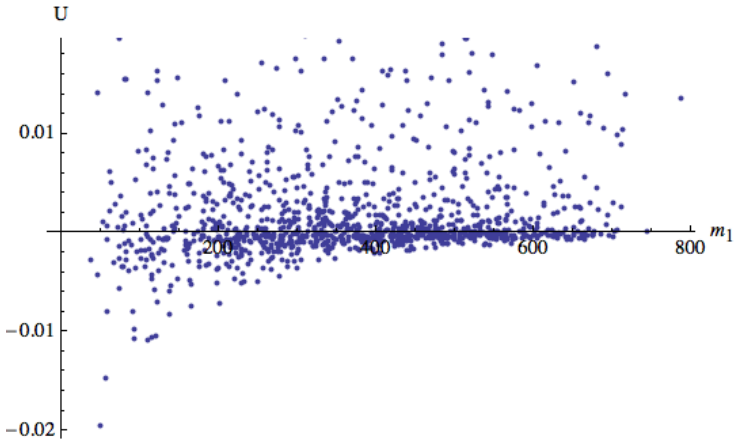

Figure 4.12: A plot of values generated for U and m_1. As m_1 increases, the minimum value for U increases and the maximum value for U stays roughly the same. These parameters display a mild correlation.

Parameters which displayed strong correlations are displayed in Figs. 4.13 and 4.14. The similarity between these two plots are a result of the direct correlation of W and V as displayed in Fig. 4.10.

4.2.3 Correlation of the Oblique Parameters and $m_{H^\pm}$

All parameters were analyzed for correlations. The relationship of the oblique parameters with m_2 and m_3 displayed very weak if not negligible correlations. Although there appeared to be correlations between $m_{1,2,3}$, these were an artifact of the ordering $m_1 < m_2 < m_3$. An example of this 'correlation' is displayed in Fig. 4.15.

The charged Higgs $m_{H^\pm}$ displayed no correlation with any of the uncharged Higgs $m_{1,2,3}$ but displayed interesting correlations with S, T, U and X. These correlations are displayed in Figs. 4.16-4.19. To maintain consistency, they have been categorized into mild, strong, and direct correlations. This categorization is displayed in Table 4.3.

Table 4.3: The levels of correlation for comparisons of $m_{H^\pm}$ with $m_{1,2,3}$ and the oblique parameters. Figs. 4.16-4.19 display these levels of correlations.

Correlation Level	Parameters
None	$m_{1,2,3}$, W, V
Mild	S
Strong	T, U
Direct	X

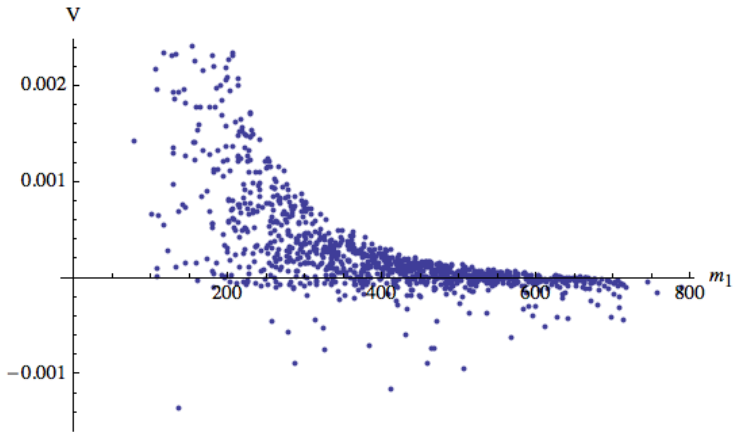

Figure 4.13: A plot of values generated for V and m_1. As m_1 increases, the V decreases exponentially. Because W and V are directly correlated, the plot of m_1-W is almost identical. These parameters display a strong correlation.

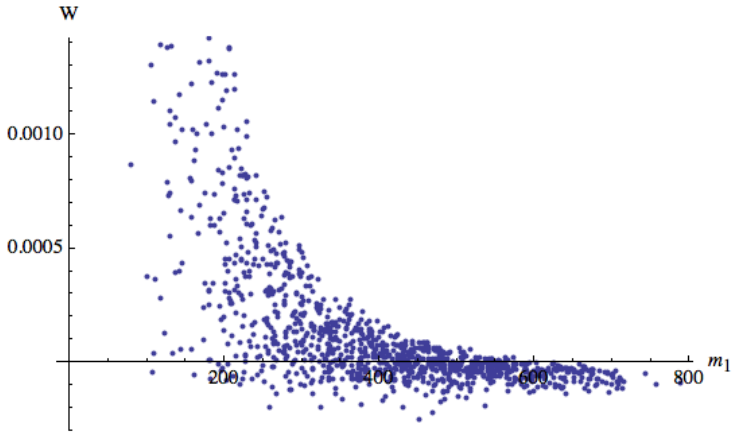

Figure 4.14: A plot of values generated for W and m_1. As m_1 increases, the W decreases exponentially. Because W and V are directly correlated, the plot of m_1-V is almost identical. These parameters display a strong correlation.

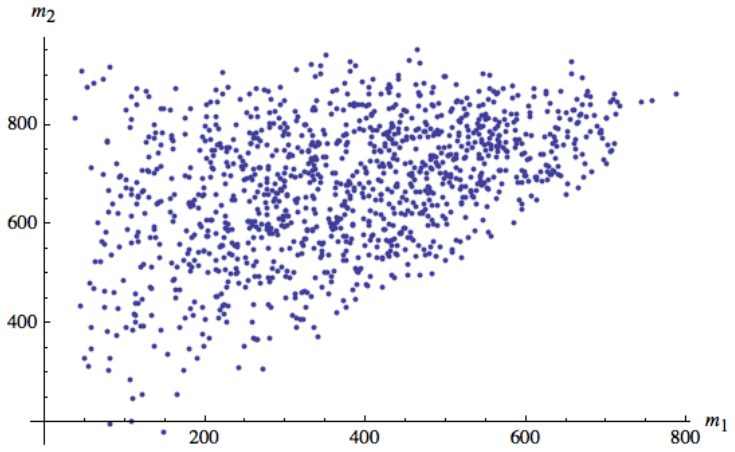

Figure 4.15: A plot of values generated for m_2 and m_1. As m_1 increases, the range of values for m_2 decreases. This 'correlation' is an artifact of the demand that $m_1 < m_2 < m_3$.

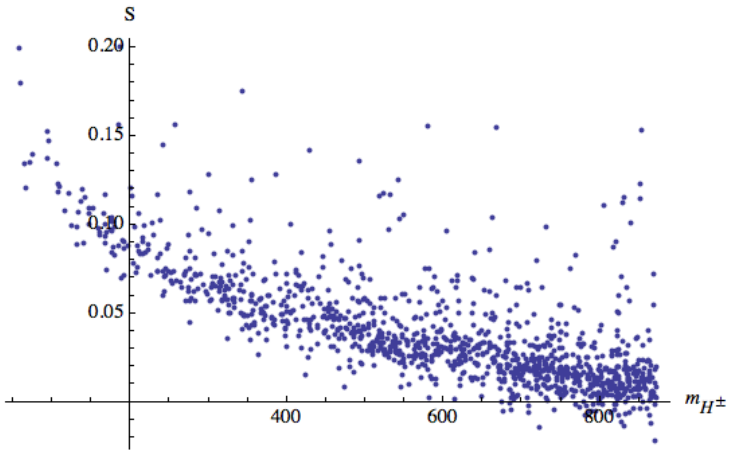

Figure 4.16: A plot of values generated for $m_{H^\pm}$ and S. These parameters display a mild correlation.

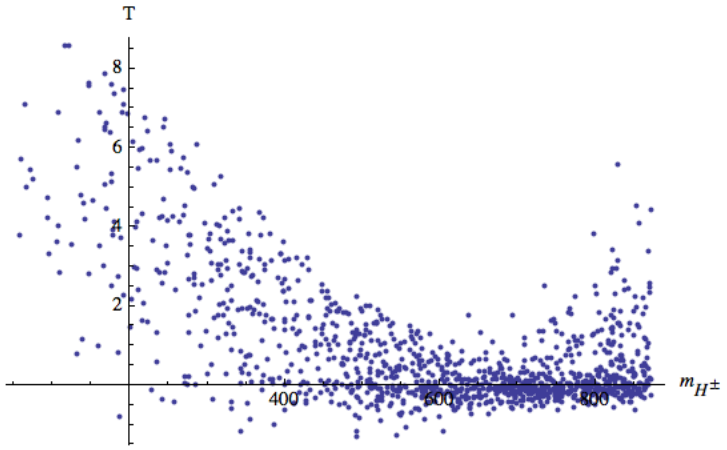

Figure 4.17: A plot of values generated for $m_{H^\pm}$ and T. These parameters display a strong correlation.

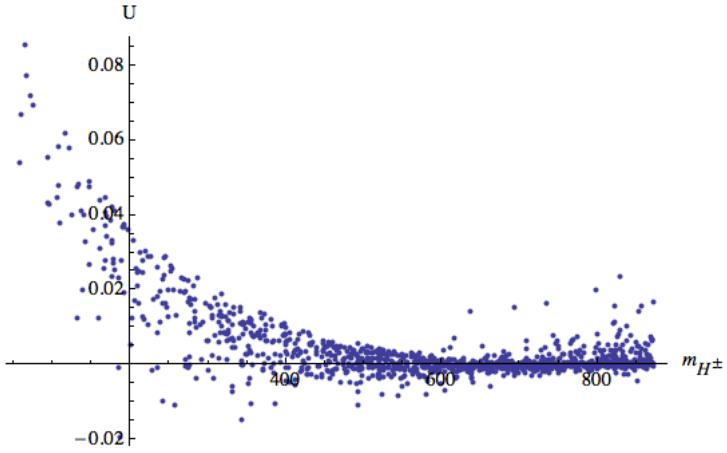

Figure 4.18: A plot of values generated for $m_{H^\pm}$ and U. These parameters display a strong correlation.

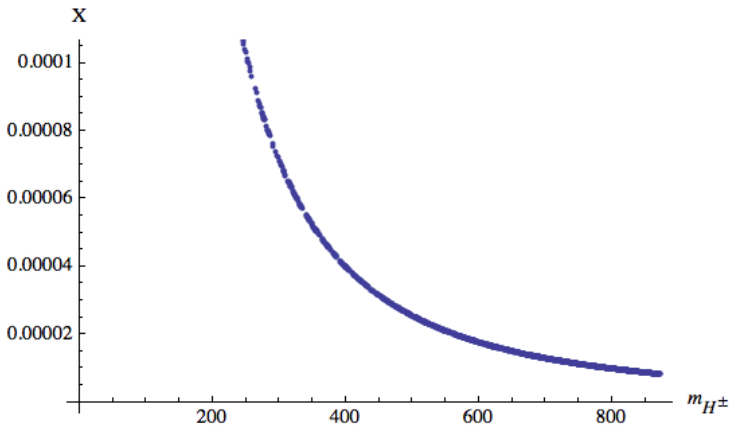

Figure 4.19: A plot of values generated for $m_{H^\pm}$ and X. These parameters display a direct correlation.

The apparent upper boundary for $m_{H^\pm}$ of ≈ 880 GeV as apparent in Figs 4.16-4.19 was found to be related to the theoretical upper bounds of Table 3.1. This relationship is discussed in greater detail in Section 4.3.2.

4.3 Adjusting the Theoretical Upper Bounds

4.3.1 Effect on the Oblique Parameters

To determine its effect on the oblique parameters, the theoretical upper bounds for Z_1, $\mathrm{Re}(Z_6 e^{-i\theta_{23}})$, $\mathrm{Im}(Z_6 e^{-i\theta_{23}})$, $\mathrm{Re}(Z_5 e^{-2i\theta_{23}})$, $\mathrm{Im}(Z_5 e^{-2i\theta_{23}})$, Z_{34}, and Z_3 were adjusted to $\frac{1}{10}$, $\frac{1}{2}$, 2 and 10 the magnitude of their original bounds. The original unitarity bounds are displayed in Table 3.1. The new unitarity bounds are displayed in Table 4.4.

Table 4.4: The new applied limits of the parameters Z_1, $\mathrm{R}(Z_6)$=$\mathrm{Re}(Z_6 e^{-i\theta_{23}})$, $\mathrm{I}(Z_6) = \mathrm{Im}(Z_6 e^{-i\theta_{23}})$, $\mathrm{R}(Z_5) = \mathrm{Re}(Z_5 e^{-2i\theta_{23}})$, $\mathrm{I}(Z_5) = \mathrm{Im}(Z_5 e^{-2i\theta_{23}})$, $Z_{34} = Z_3 + Z_4$, and Z_3. They are $\frac{1}{10}$, $\frac{1}{2}$, 2 and 10 of their values in Table 3.1.

$\frac{1}{10}$	$\frac{1}{2}$	2	10
$\lvert Z_1\rvert < \frac{2}{5}\pi$	$\lvert Z_1\rvert < 2\pi$	$\lvert Z_1\rvert < 8\pi$	$\lvert Z_1\rvert < 40\pi$
$\lvert Z_3\rvert < \frac{4}{5}\pi$	$\lvert Z_3\rvert < 4\pi$	$\lvert Z_3\rvert < 16\pi$	$\lvert Z_3\rvert < 80\pi$
$\lvert Z_3 + Z_4\rvert < \frac{4}{5}\pi$	$\lvert Z_3 + Z_4\rvert < 4\pi$	$\lvert Z_3 + Z_4\rvert < 16\pi$	$\lvert Z_3 + Z_4\rvert < 80\pi$
$\lvert \mathrm{R}(Z_5)\rvert < \frac{1}{5}\pi$	$\lvert \mathrm{R}(Z_5)\rvert < \pi$	$\lvert \mathrm{R}(Z_5)\rvert < 4\pi$	$\lvert \mathrm{R}(Z_5)\rvert < 20\pi$
$\lvert \mathrm{I}(Z_5)\rvert < \frac{1}{5}\pi$	$\lvert \mathrm{I}(Z_5)\rvert < \pi$	$\lvert \mathrm{I}(Z_5)\rvert < 4\pi$	$\lvert \mathrm{I}(Z_5)\rvert < 40\pi$
$\lvert \mathrm{R}(Z_6)\rvert < \frac{1}{5}\pi$	$\lvert \mathrm{R}(Z_6)\rvert < \pi$	$\lvert \mathrm{R}(Z_6)\rvert < 4\pi$	$\lvert \mathrm{R}(Z_6)\rvert < 40\pi$
$\lvert \mathrm{I}(Z_6)\rvert < \frac{1}{5}\pi$	$\lvert \mathrm{I}(Z_6)\rvert < \pi$	$\lvert \mathrm{I}(Z_6)\rvert < 4\pi$	$\lvert \mathrm{I}(Z_6)\rvert < 40\pi$

This adjustment produced two noticeable effects. The most clear effect was a change in the magnitude of values for T, V, W, and X, but not S and U. The approximate change in magnitude of T, V, W, and X parameters are displayed in Tables 4.5-4.6 and in Figs. 4.20-4.23. Figs. 4.20-4.23 represent 4 different data sets of ≈ 620 data points.

The second noticeable effect was that adjusting the theoretical upper bounds by a factor of 10 caused the 'direct correlation' between V and W to go away completely. This means that their 'direct correlation' was an artifact of the theoretical limits. The effect is clear in the comparison of Figs. 4.10 and 4.23.

Excluding the case of V and W, the general correlation between each pair of parameters remained almost identical in spite of the change in magnitude of T, V, W, and X. This effect is clear in the comparison of Figs. 4.2 and 4.24. Furthermore, in spite of a change of $\frac{1}{10}$ or 10 times the original theoretical upper bounds of Table 3.1, the ratio of potential data sets of the form $\{m_1, m_2, m_3, m_{H^\pm}, S, T, U, V, W, X\}$ and realistic results remained constant. Recalling the conditions of Eqn. 4.1, this means that for 10,000 potential data sets, one typically produces ≈ 620 realistic results.

Table 4.5: The effect of adjusting the theoretical upper limits of the parameters Z_1, $\mathrm{Re}(Z_6 e^{-i\theta_{23}})$, $\mathrm{Im}(Z_6 e^{-i\theta_{23}})$, $\mathrm{Re}(Z_5 e^{-2i\theta_{23}})$, $\mathrm{Im}(Z_5 e^{-2i\theta_{23}})$, Z_{34}, and Z_3 on the range of possible values for T, V, W, and X. These values exhibit the change of the theoretical limits represented in Table 4.4. These results were generated from a random set of ≈1200 observables and are displayed visually in Figs. 4.20 and 4.22.

	0.1	0.5	1
T	$(-0.21, 0.74)$	$(-0.55, 4.1)$	$(-1.16, 8.2)$
V	$(-0.0080, 0.12)$	$(-0.0079, 0.040)$	$(-0.0041, 0.040)$
W	$(-0.0016, 0.078)$	$(-0.00043, 0.025)$	$(-0.00021, 0.025)$
X	$(8.4 \times 10^{-5}, 0.0033)$	$(-1.7 \times 10^{-5}, 0.0032)$	$(8.35 \times 10^{-6}, 0.0027)$

Table 4.6: The effect of adjusting the theoretical upper limits of the parameters Z_1, $\mathrm{Re}(Z_6 e^{-i\theta_{23}})$, $\mathrm{Im}(Z_6 e^{-i\theta_{23}})$, $\mathrm{Re}(Z_5 e^{-2i\theta_{23}})$, $\mathrm{Im}(Z_5 e^{-2i\theta_{23}})$, Z_{34}, and Z_3 on the range of possible values for T, V, W, and X. These values exhibit the change of the theoretical limits represented in Table 4.4. These results were generated from a random set of ≈1200 observables and are displayed visually in Figs. 4.21 and 4.23.

	1	2	10
T	$(-1.16, 8.2)$	$(-1.8, 18)$	$(-8.1, 98)$
V	$(-0.0041, 0.040)$	$(-0.0050, 0.046)$	$(-0.011, 0.0055)$
W	$(-0.00021, 0.025)$	$(8.3 \times 10^{-4}, 0.03)$	$(-0.031, 0.012)$
X	$(8.35 \times 10^{-6}, 0.0027)$	$(4.2 \times 10^{-6}, 0.0014)$	$(8.3 \times 10^{-7}, 2.1 \times 10^{-4})$

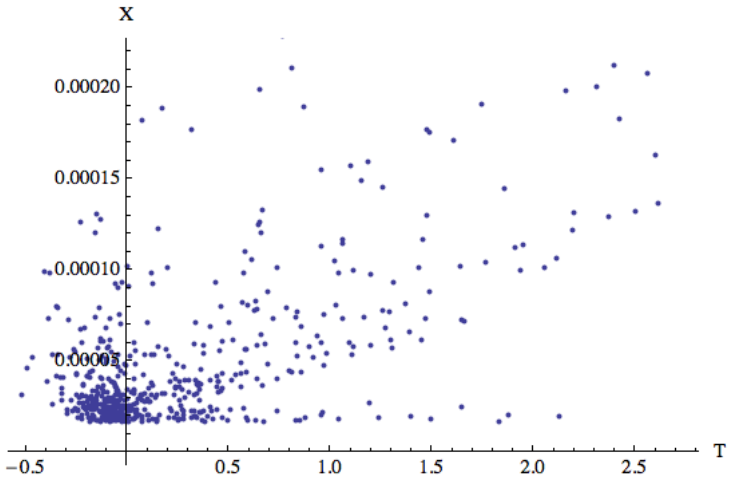

Figure 4.20: A plot of values generated for X and T with the theoretical upper bounds adjusted by a factor of $\frac{1}{2}$. Comparing this to Fig. 4.8 and 4.21, one sees a change in magnitude of the parameters, but no change in overall shape in the parameter space.

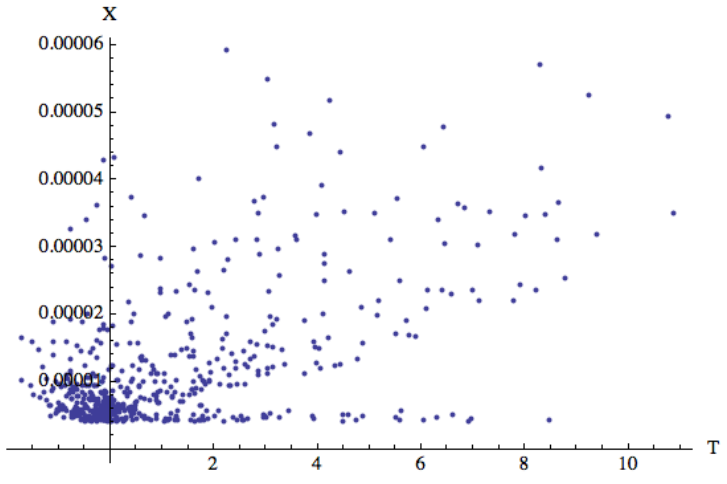

Figure 4.21: A plot of values generated for X and T with the theoretical upper bounds adjusted by a factor of 2 . Comparing this to Fig. 4.8 and 4.20, one sees a change in magnitude of the parameters, but no change in overall shape in the parameter space.

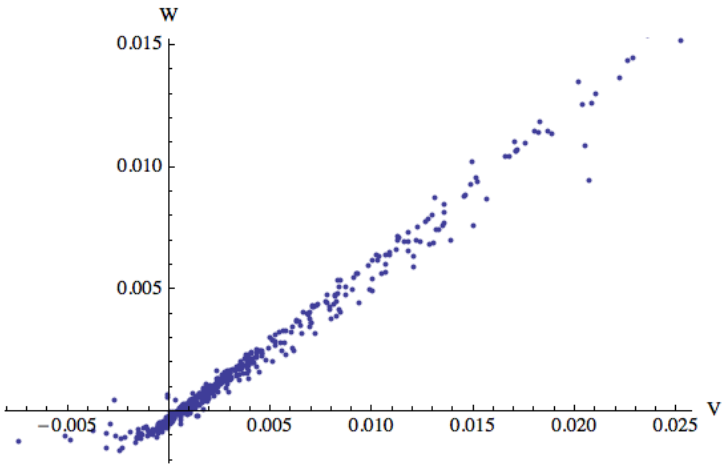

Figure 4.22: A plot of values generated for W and V with the theoretical upper bounds adjusted by a factor of 0.1. Comparing this to Fig. 4.10, one sees a change in magnitude of the parameters, but no change in overall shape in the parameter space.

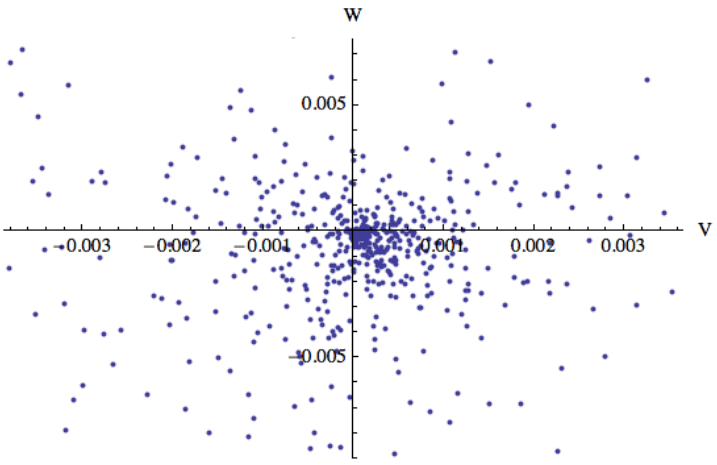

Figure 4.23: A plot of values generated for W and V with the theoretical upper bounds adjusted by a factor of 10. Comparing this to Fig. 4.10 and 4.22, one sees a change in magnitude of the parameters. Furthermore, the correlation between the two parameters is lost. These are the only two parameters to experience this change.

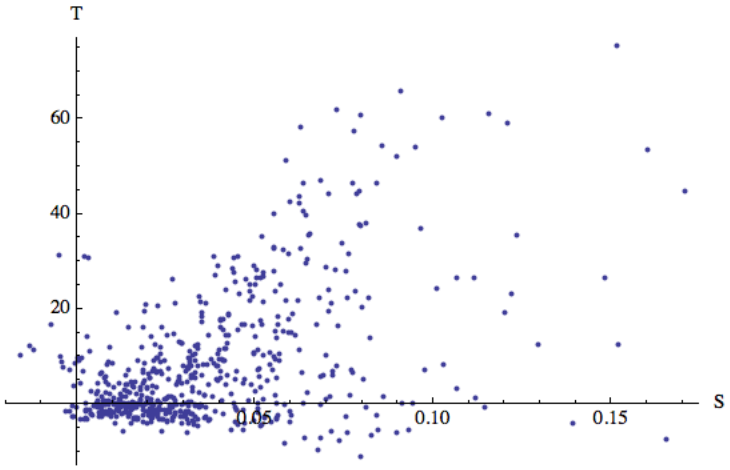

Figure 4.24: A plot of values generated for T and S with the theoretical upper bounds adjusted by a factor of 10. Comparing this to Fig. 4.2, one sees a change in magnitude of T but not S. However, the general correlation between the two remain constant. This effect was the same for every pair of parameters except W and V, wich diverged from their correlation when the theoretical boundary limits were increased by a factor of 10.

4.3.2 Effect on the Higgs particles $m_{1,2,3,H^{\pm}}$

Adjusting the unitary bounds by a factors of $\frac{1}{10}$, $\frac{1}{2}$, 2, and 10 was shown to have an effect upon the range of T, V, W, and X, and the correlation of W and V. This effect was discussed in section 4.3.1. However, it was also found that adjusting the unitary bounds had an effect upon the range of values for $m_{1,2,3,H^{\pm}}$.

This effect was determined by adjusting the theoretical upper bounds by factors of $\frac{1}{10}$ and 10 as displayed in Table 4.4. Overall, these adjustments changed the range of $m_{1,2,3,H^{\pm}}$ according to Table 4.8 and 4.9. The original range of values for $m_{1,2,3,H^{\pm}}$ is displayed in Table 4.7.

Despite the change in range of the parameters, there was no change in the shape of the correlation for any pair of parameters except for V-m_1 and W-m_1. Comparing Fig. 4.15 with 4.25 displays a change of range of the parameters but not an overall change in correlation. This recalls the results from Section 4.3.1. The change of V-m_1 and W-m_1 as displayed in Fig. 4.26, was attributed to the change in the V and W parameters rather than m_1. This argument becomes clear in the comparison of W-V as displayed in Figs. 4.10, 4.22, and 4.23.

As mentioned in section 4.3.1, adjustments to the theoretical upper bounds did not decrease or increase the number of observable data points significantly. Furthermore, these adjustments did not change the correlations between the parameters except in the case of V and W.

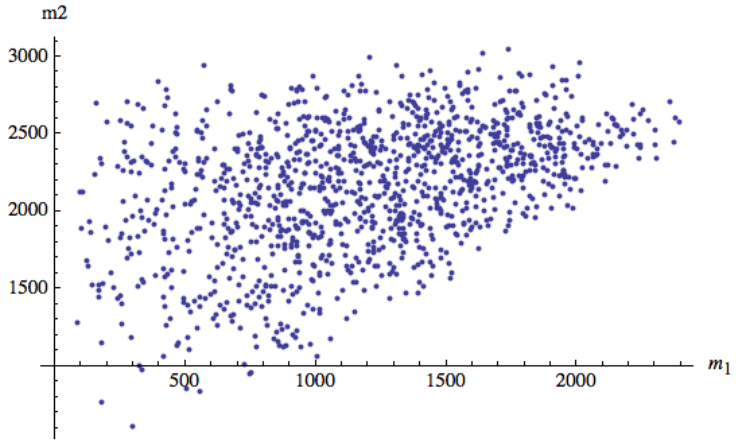

Figure 4.25: A plot of values for m_2 and m_1 with unitarity bounds adjusted by a factor of 10 as in Table 4.4. Compare this plot to Fig. 4.15 with no adjustment. There is not change in the overall shape, only in the range of values. Every parameter except V and W displayed this effect.

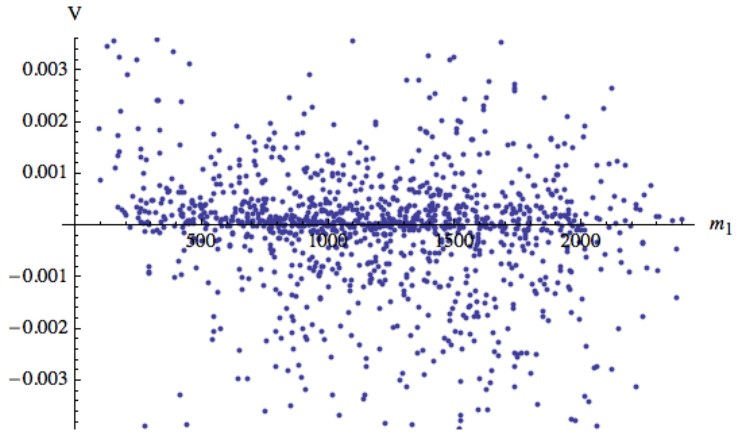

Figure 4.26: A plot of values for V and m_1 with unitarity bounds adjusted by a factor of 10 as in Table 4.4. Compare this plot to Fig. 4.13 with no adjustment. The correlation which previously existed is absent. The effect is similar for W-m_1.

Table 4.7: The range of values of $m_{1,2,3,H^{\pm}}$ using the original theoretical upper bounds of Table 3.1. Compare these values to Table 4.8 and 4.9. This data set used a random set of 1220 observables.

Higgs Mass	Max Value (GeV)	Min Value (GeV)	Range (GeV)
m_1	759.2	18.03	741.1
m_2	973.7	231.3	742.5
m_3	1114	487.0	626.6
$m_{H^{\pm}}$	872.8	51.74	821.0

Table 4.8: The changes to $m_{1,2,3,H^{\pm}}$ as a result of adjusting the theoretical upper bounds by a factor of $\frac{1}{10}$. Compare these values to Table 4.7 and 4.9. This data set used a random set of 1147 observables.

Higgs Mass	Max Value (GeV)	Min Value (GeV)	Range (GeV)
m_1	253.14	10.43	243.71
m_2	306.4	79.36	227.1
m_3	352.4	176.5	175.8
$m_{H^{\pm}}$	276.1	50.0	226.1

Table 4.9: The changes to $m_{1,2,3,H^{\pm}}$ as a result of adjusting the theoretical upper bounds by a factor of 10. Compare these values to Table 4.7 and 4.8. This data set used a random set of 1243 observables.

Higgs Mass	Max Value (GeV)	Min Value (GeV)	Range (GeV)
m_1	2620	37.63	2582
m_2	2980	737.7	2247
m_3	3514	1542	1972
$m_{H^{\pm}}$	2759	70.30	2689

Recalling the discussion of the upper limit of $m_{H^{\pm}}$ from Section 4.2.3, adjusting the theoretical upper bounds by factors of $\frac{1}{10}$ and 10 were shown to decrease or increase the upper limit of $m_{H^{\pm}}$, but the limit itself was always present. As a point of comparison, adjusting the theoretical upper bounds by a factor of 100 did not eliminate the upper limit but only increased its magnitude. A plot of T and $m_{H^{\pm}}$ is displayed in Fig. 4.27. This plot is roughly identical to a plot with the original theoretical upper bounds (Fig 4.17) except for a change in the magnitude and range of values for T and $m_{H^{\pm}}$. Consistent with a previous observation from Section 4.3.1, adjusting the theoretical upper bounds by a factor of 100 did not change the number and ratio of realistic data points to potential data points. For Fig. 4.27, for 10,000 potential data points, only 616 matched the conditions from Eqn. 4.1, and therefore could be considered realistic.

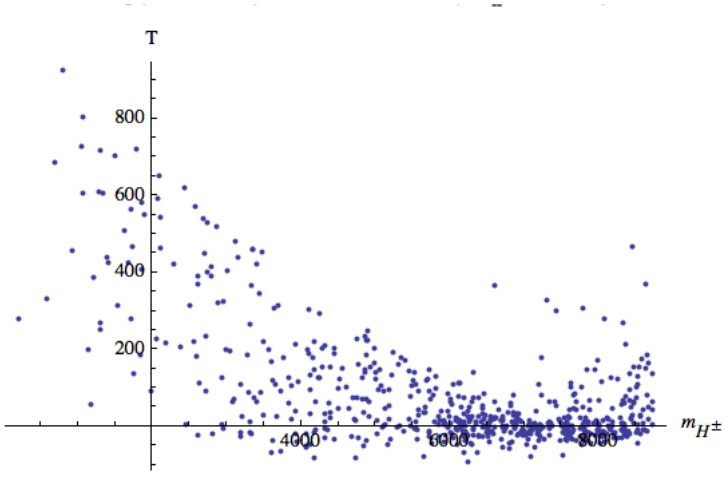

Figure 4.27: A plot of values for T and $m_{H^\pm}$ with the theoretical upper bounds of Table 3.1 adjusted by a factor of 100. Comparing this to Fig. 4.17, we see a change in magnitude of both parameters but not a change in overall correlation.

Chapter 5

Sonification

5.1 Introduction and Motivation

In the discipline of theoretical physics, computer technology has contributed immensely to rapid data acquisition. For the current experiment, production of numerical results took only minutes despite incredibly complex computation. However, the meaning of any set of data can be understood only if it can be effectively perceived. For this purpose, our visual perception has been used almost exclusively. Without comparing parameters visually through the use of two-dimensional list-plots as in Section 4.1, the data would be perceptually stagnant: approximately 620 sets of 10 numbers {S, T, U, V, W, X, m_1, m_2, m_3, $m_{H^\pm}$}.

Visual graphs have developed over time as a simple and accurate means to express information and have been used effectively in the present experiment. However, as computer processing power has blossomed within the past 30 years, new techniques have developed which offer an alternative medium of expression. Our auditory perception remains a largely untapped resource for this purpose and may provide a clear advantage in the representation of complex and high-dimensional data.

In this context, Sonification has emerged as an international field promoting new and exciting display techniques. Sonification is defined as the use of non-speech audio to convey information. A simple and well-known example is the Geiger counter, a device which represents the radiation level in its immediate vicinity using audible clicks which vary in number and frequency. Although sometimes Sonification is applied independently of visual display, it also works very well as a supplement. Among its other functions, it is helpful in the sciences where complex or high-dimensional data abound. In this environment, as in others, Sonification brings new insight to data through a unique, complex, and perhaps more complete experience. In general, its purpose is to facilitate human-computer interaction through optimal understanding and application of our aural perception.

Sonification is an interdisciplinary field drawing on support from computer science, the physical sciences, psychology and music. Computer engineers develop sound synthesis software for the transformation of numerical data into sound. In turn, scientists apply these programs as an exploratory tool in data analysis. Psychologists ask which techniques are most effective given our auditory perception. Musical understanding provides a cognitive structure and broad palette for creative sonic architecture.

With 10 observable parameters S, T, U, V, W, X, m_1, m_2, m_3, $m_{H^\pm}$, and 7 theoretical parameters [Z_1, Re($Z_6 e^{-i\theta_{23}}$), Im($Z_6 e^{-i\theta_{23}}$), Re($Z_5 e^{-2i\theta_{23}}$), Im($Z_5 e^{-2i\theta_{23}}$), Z_{34}, and Z_3], the 2HDM serves as an instance of complex, high-dimensional data. While it is possible to display high dimensionality visually (e.g., color, symbol size, shape) it is often difficult to interpret. Sonification provides the potential of displaying this high-dimensionality as a sonic experience. At minimum, sonification provides a complementary resource to visual display. At its best, instead of viewing these 17 related parameters as 136 two-dimensional list plots, they might conceivably be experienced in a single sound space.

5.2 Perceptual Resources

Auditory perception functions very differently from visual perception. While visual perception is used extensively by most humans, human auditory perception is naturally used to convey complex linguistic content. When thinking of the somewhat arbitrary collection of sounds which create meaning in a natural language, a very narrow range of our auditory perception provides easy understanding and expression for the majority of linguistic mental content. Although sound may offer a broad palette of resources to convey data, an understanding of our auditory perception is fundamental to successful sonification.

In the present experiment, pitch, loudness, spatialization, timbre, duration, and time scale were manipulated as perceptual resources for data representation. Table 5.1 links these resources with a corresponding qualitative question to help understand its use. Although there are undoubtably other resources available for auditory representation, they were not used. The addition of timbre (tone color), duration, and time scale offered a considerable step forward from previous experience [5] and the resources of Table 5.1 were thought to be sufficient for effective representation of the desired data set.

5.3 Comparing Sonification Programs

Two programs were employed as potential platforms for sonification. 'Mathematica' had been used successfully for the sonification of chaotic attractors [5] and was explored first. However, ultimately 'SuperCollider' was chosen because unlike Mathematica, its primary function is sound synthesis and it therefore offered more sonic resources.

Table 5.1: A table of perceptual resources used in the present experiment to express data through sound.

Perceptual Resource	Qualitative Question
Pitch	How high or low was the sound?
Loudness	How loud or soft was the sound?
Spatialization	Where was the source of the sound?
Timbre	What did it sound like?
Duration	How long did the sound last?
Time Scale	How long since the last sound?

Mathematica provides for sound generation through arbitrary waveform synthesis from functions and data: (i.e., the 'Play' function), as well as symbolic note-based MIDI sound synthesis (i.e., the 'SoundNote' function). MIDI stands for 'Musical Instrument Musical Interface,' and is essentially a database of instrument like sounds. After using each function, certain limitations became apparent and SuperCollider became the obvious choice for successful sonification.

The 'Play' function is the more flexible tool for sound synthesis. With this function, an arbitrary waveform can be generated from any function which evolves in time. The frequency and amplitude of the waveform are relatively easy to control and the use of multiple stereo channels is also available. Because data was generated in the form of lists in the present experiment, it was necessary to create functions to correspond to the data lists. After attempting to develop functions which adequately represented the correlations discussed in Section 4.1, it became clear that these functions were not able to capture essential information, such as the density of values within a particular region. Furthermore, not all correlations could be adequately described in terms of functions. An example of a correlation which does not lend itself well to a function representation is U and S as displayed in Fig. 4.3. This plot has a high density of points near the origin and the range of values for U increases with S. It is not clear what function could adequately describe this correlation.

Unlike 'Play', the 'SoundNote' function is well adapted to create sound through the use of lists. This feature made it clearly preferable to 'Play'. However, there is considerably less flexibility in sound synthesis. 'SoundNote' uses MIDI-style sound synthesis, which means that notes will sound music-like. Although there are certain perceptual advantages to music-like sounds, these sounds cannot be altered or distorted. This restriction means that the timbre remains constant or varies between certain music-like notes. Either of these options places restrictions on its use as a perceptual resource. Another disadvantage of 'SoundNote' is that it offers no option for multi-channel stereo output. Therefore, unlike 'Play,' the sound synthesis cannot involve spatialization as a perceptual resource. This restriction means that the sound cannot "move." However, perceptual dimensions such as duration, loudness, and pitch could relatively easily be controlled. This made correlations between three parameters

relatively easy to sonify.

5.4 Experimentation

Although 17 parameters exist, for the sake of simplicity, only the 10 observable parameters were analyzed. Although these parameters are dependent upon the theoretical parameters, the observables were the focus of the present experiment. Visual 2-D plots are displayed and discussed in Section 4.1. To find the correlations between the 10 observable parameters, 45 2-D plots were analyzed (ie. m_1-S, V-W).

The correlation between the parameters SVWm_1, SVW$m_{H^\pm}$, TUXm_1, and TUX$m_{H^\pm}$ were chosen for sonification. These groups were chosen firstly because of the mutual correlations between the S,V, and W parameters as displayed in Figs. 4.4 and 4.10, as well as the mutual correlations between T, U, and X as displayed in Figs. 4.9, 4.8, and 4.7. The variable m_1 was chosen because of its importance as the least Higgs mass, the most likely particle to be observed at the LHC. The variable $m_{H^\pm}$ was chosen because of its interesting correlations with the oblique parameters S and T as displayed in Figs. 4.16 and 4.17. Because m_1 lacks correlation with these variables the result was two sound files identical in some respects but clearly different in others.

Without a specific time dependence of any of the variables, one must be chosen as a substitute. Unlike visual display, auditory display must have an explicit time relation. A sonic space must evolve in time or it cannot exist at all. The the sonic evolution might be stagnant (i.e. a constant tone of arbitrary duration), but a time relation must exist. The parameters S and T were chosen as substitutes. Therefore, for the groups SVWm_1 and SVW$m_{H^\pm}$, the values of V, W, and m_1 or $m_{H^\pm}$ evolve in time proportionally to their relation with S. Similarly, for the groups TUXm_1 and TUX$m_{H^\pm}$, values of U, X, and m_1 or $m_{H^\pm}$ evolve in time proportionally to their relation with T.

5.5 Using SuperCollider

As mentioned in Section 5.3 Mathematica proved insufficient as a tool for sonification of the present data set. The program 'SuperCollider' offered the clear choice for sonification, but was explored only after Mathematica because it required learning a new programming language. Using the help files, much was learned. However, lack of programming experience and time constraints provided clear limitations to its use. Fortunately, Florian Grond of the Ambient Intelligence Group at Bielefeld University offered an effective and compelling prototype which was modified and used as the basis for all further sonification.

Lists which ordered SVWm_1, SVW$m_{H^\pm}$, TUXm_1, and TUX$m_{H^\pm}$ with respect to S and T were exported from Mathematica as comma-sperated value (.csv) files. These files were imported by SuperCollider and each variable was normalized independently to a value between 0 and 1. With these parameters in

mind, an algorithm for sound synthesis was developed by Florian Grond using the SuperCollider programming language. All of the resources of Table 5.1 were employed. Therefore each element of the list (i.e. SVWm_1) corresponded to a sound of particular pitch, loudness, spatialization, timbre, duration, and time scale.

Although many of the resources of Table 5.1 are relatively easy to explain, timbre is complex and requires additional discussion. In the SuperCollider programming language, 'Unit Generators' (UGens) are a fundamental tool for sound synthesis. A simple example of a UGen is 'SinOsc,' a perfect sine wave. Its arguments include frequency of oscillation, phase, and amplitude. These arguments can be adjusted to vary with time with respect to some variable.

For the present experiment, sound synthesis involved the 'Formant' UGen. This UGen generates a set of harmonics around a formant frequency at a given fundamental frequency. Formants can be thought of as important to distinguishing between particular vowel sounds in human speech and singing. While keeping a fundamental tone, vowels nevertheless sound different because they have different formant frequencies. The arguments of the 'Formant' UGen include fundamental frequency, formant frequency, and pulse width frequency. Although all three of these arguments were used, only formant frequency and pulse width frequency were considered to correspond to timbre.

5.6 Sonification of the Oblique Parameters and m_1, $m_{H^\pm}$

Parameters from SVWm_1, SVW$m_{H^\pm}$, TUXm_1, and TUX$m_{H^\pm}$ were mapped onto the perceptual recourses from Table 5.1 in such a way as to maximize perceptual comprehension of the data sets. This mapping is displayed in Table 5.2. A 3-D list plot generated in Mathematica can be viewed in Figs. 5.1 and 5.2. For sonification, the conditions for Eqn. 4.1 were further restricted so that

$$m_{H^\pm} < 100, \text{ and} \tag{5.1}$$

$$m_1 < 100. \tag{5.2}$$

This was to limit the number of extraneous data points. Recalling Figs. 4.13 and 4.19, small values for m_1 and $m_{H^\pm}$ create values for V, W, and X which are radically different from the majority of points.

In each case, the difference in the level of correlation between S-m_1 and $m_{H^\pm}$ or T-m_1 and $m_{H^\pm}$ was found to be easily perceivable. Although duration was also used to express m_1,$m_{H^\pm}$ (see Table 5.2), the most clear difference in the soundfiles was the change in timbre over time for S-$m_{H^\pm}$ and T-$m_{H^\pm}$. There was no characteristic change in timbre in either S-m_1 or T-m_1.

The difference in correlation between S-m_1 and S-$m_{H^\pm}$ is displayed in Figs. 4.11 and 4.16. The difference in correlation between T-m_1 and T-$m_{H^\pm}$ is displayed in Figs. 4.17 and 5.3. Because there is no correlation between T and m_1, Fig. 5.3 is not displayed in section 4.1. For Figs. 4.11, 4.16, 4.17, and 5.3, recall

that SVWm_1, SVW$m_{H^\pm}$, TUXm_1, and TUX$m_{H^\pm}$ were ordered with respect to increasing values of S or T. The difference between SVW and TUX was not as easy to differentiate, but careful listening could always indicate which was the correct data set. The most obvious auditory difference between the data sets is visually apparent in Figs. 5.1 and 5.2. There is a collection of points in the lower right hand region of SVW that is not present in TUX.

Table 5.2: A table of perceptual resources used in the present experiment to express data through sound. 'Mapping' refers to which parameter of the data set TUX or SVW corresponds to the perceptual resource (i.e. S or T, V or U)

Perceptual Resource	Mapping
Pitch	U/V
Loudness	X/W
Spatialization	T/S
Timbre	m_1, $m_{H^\pm}$
Duration	m_1, $m_{H^\pm}$
Time Scale	X/W

5.7 Perceptual Experiment

Understanding our auditory perception is absolutely necessary for effective sonification. The mapping displayed in Table 5.2 was not believed to be the most effective sonification of the present data set, but it was thought to be sufficient. Despite similarities in the shape and contour of SVW and TUX (both occupy roughly the same space), each sonification was differentiable. Especially clear was the difference between the data sets SVWm_1 and SVW$m_{H^\pm}$, or similarly, TUXm_1 and TUX$m_{H^\pm}$. The difference was attributed to the level of correlation between S or T and m_1 or m_H.

Recognizing the importance of perception to effective sonification, a very brief and simple perceptual experiment was undertaken with a group of undergraduate students in the context of an introductory-level physics class. Although a rigorous testing of mapping techniques would be desirable, given constraints in time and experience, this level of perceptual testing was not undertaken for the present experiment. The purpose of the experiment was to test the effectiveness of mapping spatialization, pitch, and loudness onto particular parameters. Therefore, only three parameters were necessary and in the interest of simplicity, the data sets SVWm_1, SVW$m_{H^\pm}$, TUXm_1, and TUX$m_{H^\pm}$ were reduced to SVW and TUX. The six possible mappings of SVW and TUX are displayed in Table 5.3.

Because the experiment was designed to take place within the timeframe of 10 minutes at the beginning of class, only two mappings from Table 5.3 were selected, Mapping #2 and #6. These mappings were thought to be the most effective of the six by myself and Dr. O'Neil. Using these mappings, four ≈ 20

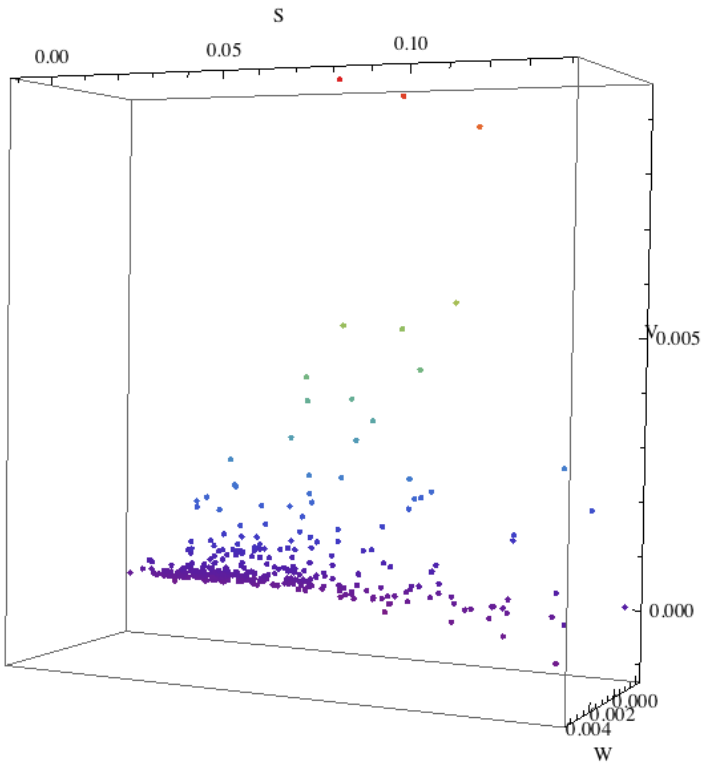

Figure 5.1: A plot of 343 values for S, V, and W with the original theoretical upper bounds of Table 3.1. Color is being used to perceptually reinforce the X parameter. Each parameter in this set was paired with a perceptual resources from Table 5.1. This mapping is displayed in Table 5.2.

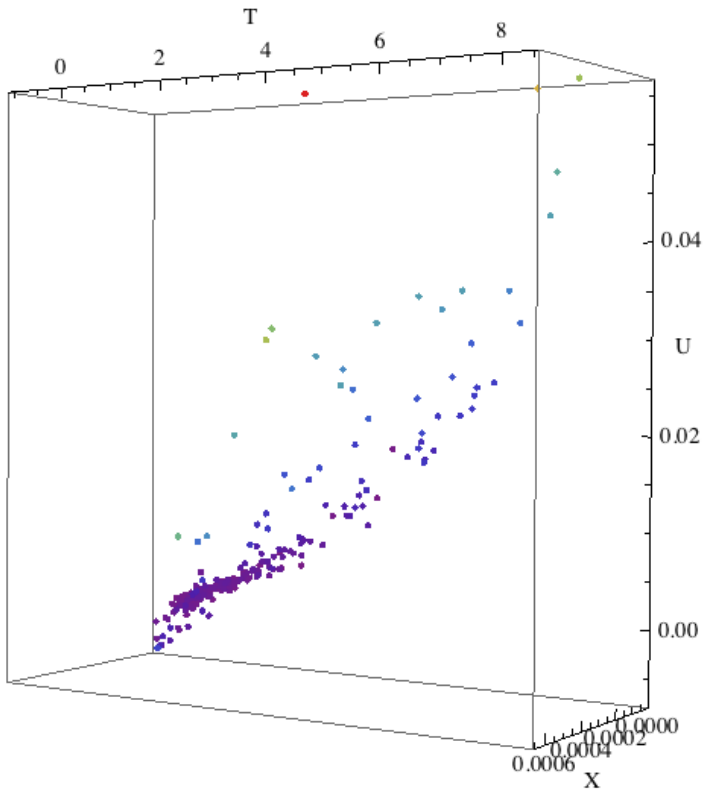

Figure 5.2: A plot of 343 values for T, U, and X with the original theoretical upper bounds of Table 3.1. Color is being used to perceptually reinforce the X parameter. Each parameter in this set was paired with a perceptual resources from Table 5.1. This mapping is displayed in Table 5.2.

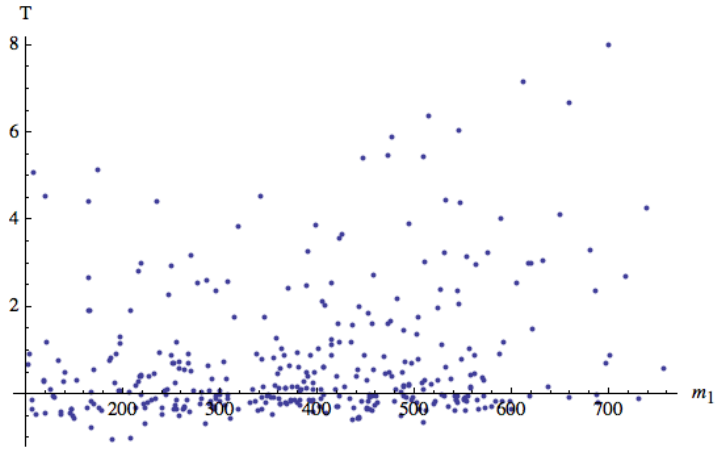

Figure 5.3: A plot of 343 values for T and m_1 with the original theoretical upper bounds of Table 3.1. Although there is no correlation between these two parameters, there is a correlation between T and m_H as displayed in Fig. 4.17. Given the mappings of Table 5.2, TUXm_1, and TUX$m_{H^\pm}$ will therefore sound different.

Table 5.3: A table of possible mappings of spatialization, pitch, and loudness with the data sets SVW and TUX. For the perceptual experiment, only Mapping #2 and #6 and were tested.

Parameter	S, T	V, U	W, X
Mapping #1	Spatialization	Pitch	Loudness
Mapping #2	Spatialization	Loudness	Pitch
Mapping #3	Pitch	Loudness	Spatialization
Mapping #4	Pitch	Spatialization	Loudness
Mapping #5	Loudness	Spatialization	Pitch
Mapping #6	Loudness	Pitch	Spatialization

second sound files were created- two with SVW using mapping #2 and #6 and two for TUX using mapping #2 and #6. For each, the timbre, duration, and time scale were kept constant. The formant frequency and pulse width frequency were kept at 100Hz each. Each note lasted 0.3 seconds and a new note struck every 0.05 seconds.

After a brief introduction to the particle physics research and sonification, Figs. 5.1 and 5.2 were displayed in front of the class. After explaining how SVW and TUX would sound differently given the particular mapping technique, the two sound files were played in random order and the class was asked which was played first. This was done for both mapping #2 and #6. In the end out of 18 students in the class, 11 voted correctly for both #2 and #6.

The classroom was equipped with stereo speakers so spatialization was thought to be effectively communicated. However, there may be differences on account of where a student was sitting in the classroom. Furthermore, there is no consideration of the motivation of each student to provide the correct answer or listen carefully. Without considering these variables and others perhaps unconsidered, our results may not be significant. Nevertheless, it was surprising that a clear majority of the class voted correctly twice.

Given the small sample, it may be that this result was due to chance. If a group of 18 students voted randomly, there is a 24% chance that 11 or more would guess correctly. This result comes from the binomial expansion:

$$\mathrm{P}(11 \text{ or more}) = \frac{18!}{2^{18}} \sum_{y=11}^{18} \frac{1}{y!(18-y)!}. \tag{5.3}$$

Although these results lack the rigor of a psychology experiment, they nevertheless seem to say that neither mapping #2 or #6 were more effective. In the future, it would be interesting to note which students voted correctly each time and why. It would also be worthwhile to compare different levels of physics students to see if experience with visual graphs had any effect on correct answers. For example, Fig. 5.1 has three red points in the upper region of the graph. Could it be that these three extreme points made the correct answer obvious for some?

Chapter 6

Conclusions & Future Work

6.1 Conclusion

Theoretical calculations involving the basis-independent CP-violating Two-Higgs Doublet Model revealed correlations between the oblique parameters and the five Higgs particles $m_{1,2,3,H^{\pm}}$. Changing the theoretical bounds of Z_1, $\mathrm{Re}(Z_6 e^{-i\theta_{23}})$, $\mathrm{Im}(Z_6 e^{-i\theta_{23}})$, $\mathrm{Re}(Z_5 e^{-2i\theta_{23}})$, $\mathrm{Im}(Z_5 e^{-2i\theta_{23}})$, Z_{34}, and Z_3 by factors of $\frac{1}{10}$, $\frac{1}{2}$, 2, and 10 were found to change the range of T, V, W, X and $m_{1,2,3,H^{\pm}}$. However, these adjustments did not change the general correlations any of the parameters except in the case of V and W. The correlation of V and W was proven to be an artifact of the theoretical upper bounds and was lost at some point between an adjustment factor of 2 and 10. A disproportionate number of correlations exist between the oblique parameters and $m_{H^{\pm}}$ compared to $m_{1,2,3}$.

Sonification was proven to be effective as a means to display correlated data sets involving four parameters (SVWm_1, SVW$m_{H^{\pm}}$, TUXm_1, and TUX$m_{H^{\pm}}$). The computer program SuperCollider was found to be clearly preferable to Mathematica as a tool for sonification given this particular data set. A brief perceptual experiment revealed that particular mappings involving spatialization, pitch, and loudness were not perceptually more efficient.

6.2 Future Work

The relationships between the seven theoretical parameters Z_1, $\mathrm{Re}(Z_6 e^{-i\theta_{23}})$, $\mathrm{Im}(Z_6 e^{-i\theta_{23}})$, $\mathrm{Re}(Z_5 e^{-2i\theta_{23}})$, $\mathrm{Im}(Z_5 e^{-2i\theta_{23}})$, Z_{34}, and Z_3 and the 10 observable parameters S, T, U, V, W, X, $m_{1,2,3,H^{\pm}}$ should be explored and analyzed for correlations. Although their importance might be secondary to the observables, the present experiment is not complete without this additional analysis.

The perceptual experiment performed in this project was critically limited by time constraints. A more thorough and rigorous experiment would be valuable if not a necessity for better sonification. Further research and inquiry into auditory

perception would provide a more concrete understanding and application of the perceptual resources of Table 5.1.

The current experiment was also limited by experience with SuperCollider and Sonification in general. With more time and experience, more sophisticated sonifications could be created. In addition to displaying our data better, this level of sophistication would be consistent with that of other researchers.

6.3 Ethical Considerations

It is important to examine the potential risks of research so that unnecessary harm is avoided. The current research has no foreseeable risk of direct or indirect harm. Considering these ethical implications, this research is found it to be acceptable for publication and further inquiry.

Bibliography

[1] H. E. Haber and D. O'Neil, "Basis-independent methods for the two-Higgs-doublet Model. II: The significance of tan(beta)," Phys. Rev. D **74**, 015018 (2006) [arXiv:hep-ph/0602242].

[2] H. E. Haber. "Introductory low-energy supersymmetry," arXiv:hep-ph/9306207.

[3] D. O'Neil, "Phenomenology of the Basis-Independent CP-Violating Two-Higgs Doublet Model [Dissertation]," arXiv:0908.1363 [hep-ph].

[4] G. Passarino and M. J. G. Veltman, "One Loop Corrections For E+ E- Annihilation Into Mu+ Mu- In The Weinberg Model," Nucl. Phys. B **160**, 151 (1979).

[5] R. Winters, "Musical Mapping of Chaotic Attractors." (2009)

[6] I. Maksymyk, C. P. Burgess and D. London, "Beyond S, T and U," Phys. Rev. D **50**, 529 (1994) [arXiv:hep-ph/9306267].

[7] J. H. Christenson, J. W. Cronin, V. L. Fitch and R. Turlay, "Evidence For The 2 Pi Decay Of The K(2)0 Meson," Phys. Rev. Lett. **13**, 138 (1964).